ATOMIC OXYGEN CONSIDERATIONS FOR LEO DE-ORBIT TRAJECTORIES USING SOLAR SAILS

A Thesis

presented to

the Faculty of California Polytechnic State University,

San Luis Obispo

In Partial Fulfillment

of the Requirements for the Degree

Master of Science in Aerospace Engineering

by

Daniel Fugett

June 2017

COMMITTEE MEMBERSHIP

TITLE:	Atomic Oxygen Considerations for LEO De-Orbit Trajectories Using Solar Sails
AUTHOR:	Daniel Fugett
DATE SUBMITTED:	June 2017
COMMITTEE CHAIR:	Kira Jorgensen Abercromby, Ph. D. Associate Professor of Aerospace Engineering
COMMITTEE MEMBER:	Jordi Puig-Suari, Ph. D. Professor of Aerospace Engineering
COMMITTEE MEMBER:	Eric Mehiel, Ph. D. Professor of Aerospace Engineering
COMMITTEE MEMBER:	Katharina Gillen, Ph. D. Associate Professor of Physics

ABSTRACT

Atomic Oxygen Considerations for LEO De-Orbit Trajectories Using Solar Sails

Daniel Fugett

Solar sails have the potential to benefit many future space exploration missions, but they lack the heritage required for present-day use. To grow confidence in solar sail technology, they could be deployed on LEO satellites higher than 600 km to help de-orbit the satellite within 25 years upon mission termination. To determine how atomic oxygen would affect the solar sail, material from Lightsail-2 was tested in a thermal-energy, isotropic, atomic oxygen vacuum chamber based in the space environments laboratory in California Polytechnic State University. The sail material, aluminized Mylar, was tested for its survivability on both the coated and uncoated side, as well as tested for the optical degradation of the coated side. The uncoated side was found to be completely eroded after a fluence of 2.27 $x10^{20}$ atoms/cm^2, or ~40 days in International Space Station orbit. The coated side experienced no mass loss, but signs of significant undercutting were found with a fluence of 1.19 $x10^{21}$ atoms/cm^2, or ~200 days at station orbit. The stitches present on the coated side, meant to prevent tear propagation, eroded before the sample experienced a fluence of 4.13 $x10^{20}$ atoms/cm^2, or ~70 days at station orbit. The average total reflectivity of the material dropped by ~5% after atomic oxygen exposure, however no correlation with fluence was found. Average specular reflectivity remained unchanged after atomic oxygen exposure. The reflectivity results were impacted by wrinkling in the material, which was found to have a much larger impact than atomic oxygen exposure. These results were paired with an optimal de-orbit trajectory algorithm, developed in this thesis, to determine how atomic oxygen would affect a solar sail deployed to de-orbit an 800 km LEO satellite with a ballistic coefficient of 0.1. Using a simplified 2D orbit case, it was found that the satellite would de-orbit within 12-18 years, depending primarily on the solar activity level. The measured worst-case for optical degradation increased de-orbit time by ~6 months. Additionally, assuming that the sail material was perfectly reflecting decreased de-orbit time by 2-4 years. The amount of fluence required to erode the uncoated Mylar, and the amount required to erode the stitches, were both reached long before the satellite re-entered. It is therefore recommended that the solar sail minimize uncoated side exposure to atomic oxygen, and a more atomic oxygen-resistant stitch material be found. The fluence required to produce significant material undercutting was reached only once the satellite's orbit had degraded to below 400 km. But the undercutting was observed to structurally compromise the material; thus, future LEO solar sail mission designers must take care when balancing added performance with higher failure risk when considering the tension in the deployed sail.

ACKNOWLEDGMENTS

The author would like to thank Dr. Kira Abercromby of California Polytechnic State University for acting as the advisor of this thesis. Also, Dr. Katharina Gillen and Dr. Hans Mayer who assisted heavily in the data collection. Thanks to SpaceX and Ecliptic Enterprises for donating the materials required. Lastly, thanks to all who assisted in the Spacecraft Environments lab.

TABLE OF CONTENTS

Page

LIST OF TABLES

Page

LIST OF FIGURES

Page

1.0 Background

1.1 Solar Sails

In the early 20th century, Tsiolkovsky first articulated the idea of using light pressure from the sun to generate thrust on a spacecraft. It wasn't until 1958 that the idea started being considered in engineering practice, and the term "solar sailing" was coined. However, the idea was still not ready to be used in a mission until the 1990's. The first solar sail to ever deploy was during a ground test conducted by the German space agency, DLR, in 1999 [1]. Following that, NASA completed two different solar sail development programs for the Sunjammer mission [1]. The goal was to develop solar sail technology to Technology Readiness Level (TRL) 6, meaning system prototype tested in a relevant environment [2]. However, the final assessment showed that both programs failed to meet TRL level 5, meaning not even a component was tested in a relevant environment [2]. Sunjammer was subsequently canceled [1].

In May 2010, the Japanese space agency, JAXA, launched the first solar sailing spacecraft. The spacecraft, named IKAROS, launched into a near-Venus transfer trajectory with a square solar sail. The solar sail had thin-film solar arrays embedded inside to generate power, as well as liquid crystal devices that could be switched from diffusely to specularly reflective for attitude control. The IKAROS mission was considered a success and continues to orbit the sun to this day [1].

Meanwhile, NASA and the Planetary Society started developing Cubesat based solar sails. In 2008, NASA launched the solar sailing CubeSat, NanoSail-D, which failed shortly after launch due to a problem with the launch vehicle [1]. Its replacement, NanoSail-D2, was launched into LEO in 2010 and successfully deployed its solar sail. After 240 days on orbit, the mission ended by burning up in Earth's atmosphere [3]. The

Planetary Society's solar sailing LEO Cubesat, LightSail-1, was successfully deployed after some software malfunctions in 2015 [4]. The follow-up mission, LightSail-2, is expected to be launched in summer 2017 [5].

Solar sails are uniquely suited to be used for a variety of missions. Similar to electric propulsion, the main benefit of a solar sail is that it can provide constant, low thrust for a long duration. However, the advantage over electric propulsion is that a solar sail requires no fuel and takes up less mass and power. The disadvantage compared to electric propulsion is that a solar sail's thrust depends on both the spacecraft's distance to the sun and the spacecraft's attitude. Due to drag and difficult pointing requirements, solar sails are often considered best for missions outside the sphere of influence of the Earth [1]. Dr. Malcolm MacDonald conducted a trade study with different types of contemporary propulsion for a variety of interplanetary missions, with the goal of identifying which missions would benefit from solar sails. Table 1, from Dr. MacDonald, shows a summary of the author's trade studies, with the results organized by: missions that would benefit heavily from solar sails, missions with little benefit from solar sails, and missions with no benefit from solar sails.

Table 1. Solar Sail Potential Missions [1]

Enabled or Significantly Enhanced	Marginal Benefit	No Benefit
Non-Inertial Orbits	Venus escape at end of sample-return mission	Planetary escape at start of mission
Highly Non-Keplarian Orbits	Mercury sample-return missions	Mars Missions
Kuiper-Belt fly-through	Outer solar system planet fly-by	Outer solar system rendezvous
Solar Polar Orbiter	Transit of Gravitational Lens region	Loiter at Gravitational Lens
Interstellar Heliopause Probe	Oort Cloud	

The missions that solar sails benefit most are those which rely on constant, low-thrust systems to maintain a particular orbit, like non-inertial and non-Keplarian orbits. Missions which require a long-duration burn to achieve a high delta-V, like the solar polar orbiter mission, are also heavily benefited. In both types of long-duration missions, solar sails would be preferable to electric propulsion because sails do not require any fuel or any additional power generation, creating room on the spacecraft that can be used for more scientific instruments.

Solar sailing has a promising future for a variety of interplanetary missions. Unfortunately, the only interplanetary mission to successfully employ solar sails has been IKAROS. Many other missions have been proposed, but all were canceled because of budget-constraints or lack of confidence in the technology due to its novelty [6]. Before solar sails are employed on high risk interplanetary missions, the confidence in the technology must grow. Thus, a low-risk, cheap mission is needed to help prove that the technology is ready.

The German Aerospace Center, DLR, and ESA created a technology roadmap for solar sailing, in which multiple solar sails were to be created and tested in LEO. These tests could help demonstrate reliable deployment and attitude control mechanisms for solar sails [7]. Unfortunately, these tests were never completed because the project lost most of its funding. To ensure that project funding remains constant, a preliminary solar sailing mission should attempt an important objective in addition to developing the sailing technology. That way, solar sail technology experiences a "push" from a mission application while it is being "pulled" by a development program [1].

One idea for a low-cost mission application is to use solar sails to help de-orbit LEO objects. NASA and ESA have a requirement that every satellite in an orbit with an altitude below 2000 km must de-orbit within 25 years after the end of its mission [6]. For satellites lower than ~600 km, this can often be done by letting atmospheric drag pull the orbit down. But for higher orbits, a propulsive device is needed to ensure that the requirement is met. This can be a driving requirement in some missions, as right now it means that either a heavy chemical propulsion system or a power-hungry electrical propulsion system is needed. Having little mass and requiring no fuel or power, solar sails would be uniquely suited to this task. And, while being used to help de-orbit satellites, solar sails would also experience an increase in technology confidence, so that one day the riskier interplanetary missions could be developed [6].

ESA already has a plan to implement solar sails to help de-orbit LEO satellites. The Gossamer De-Orbit Sail has been developed and ground tested, and is hoping to be implemented on its first flight soon. The sail takes the form of a 15x15x25 cm package that weighs only 2 kg. This package can be integrated with the rest of the satellite, and

upon mission termination, the package can deploy a 25 m^2 solar sail. It is intended to help de-orbit a 700 kg, 700 km altitude satellite within 25 years [8].

For interplanetary trajectories, a solar sail would predominantly experience the radiation environment as a source of degradation. This environment has been thoroughly studied in the context of solar sails. But, if solar sails are to be used in LEO, they will experience an environment dominated by atomic oxygen. And few, if any, research papers have been published on what considerations should be taken during the design of a solar sail to prepare it for an atomic oxygen environment.

1.2 Atomic Oxygen

Atomic oxygen implies single oxygen atoms; in the Earth's upper atmosphere it is created by the photo dissociation of O_2. Any wavelength of light shorter than approximately 242 nm has enough energy to break up oxygen molecules into atomic oxygen, or AO [9]. At high altitudes, the density of gas molecules is low enough that the atomic oxygen will not recombine, but is still dense enough to cause problems for spacecraft. Figure 1 shows the approximate number density of different gas molecules at various altitudes in the year 2012 [9]. It uses the Naval Research Laboratory Mass Spectrometer Incoherent Scatter model (NRLMSISE-00). While Figure 1 illustrates the relative density of different gas species, the number density values themselves can fluctuate. Solar activity, season, local time, latitude, and variations in Earth's magnetic field all have a large impact on the exact number density of a particular gas species. To exemplify this variation, at a 400-km circular orbit it was found that, on an example surface, the total number of atomic oxygen particle collisions per year increased three-fold over a seven-year time span [9].

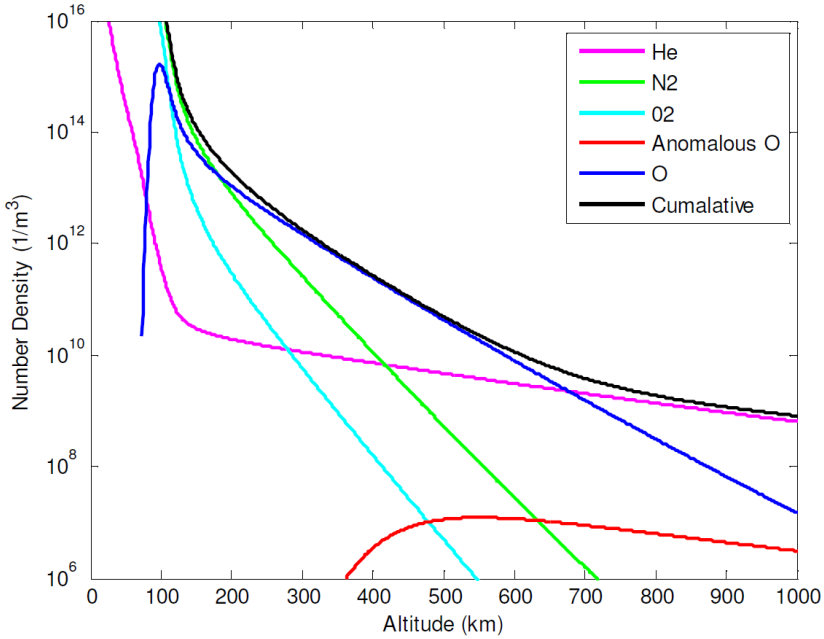

Figure 1. Number Density of Ambient Gases in Earth's Upper Atmosphere Based on NRLMSISE-00 Model [9]

Figure 1 illustrates that atomic oxygen becomes the dominant species from around 300 to 700 km in altitude. So, any spacecraft flying in this regime should prepare to experience the effects that atomic oxygen can have on spacecraft materials.

The effects of atomic oxygen were first seen after the earliest space shuttle flights [10]. The degradation experienced led to a large effort to understand the problems caused by atomic oxygen. The most severe problem is erosion. When oxygen atoms collide with a polymeric surface, a volatile reaction product is created, which then carries mass away from the surface. The polymeric material is left both structurally weakened and with a rougher topography. Additionally, the gaseous byproducts can be a source of contamination for sensitive surfaces. Another common problem with oxygen atoms is oxidation. When exposed to atomic oxygen, some materials become oxidized without eroding. This can lead to a change in the optical properties of a material, which has a large impact on its thermal properties [10].

Hydrocarbons and fluorocarbons typically experience the worst erosion. This is because those materials have the highest reaction efficiencies; that is, an oxygen atom has a relatively large chance of bonding with the surface molecules. To better understand the mechanism that atomic oxygen uses to erode material, consider a hypothetical graphite surface, similar to that shown in Figure 2. If the oxygen atom hits the surface with enough energy, it will bond with a carbon atom. That carbon atom is now being held in place with weaker bonds than it was before. If another oxygen atom strikes the bonded oxygen-carbon, the oxygen-carbon molecule will break away from the rest of the carbon structure. This process can be seen in Figure 2.

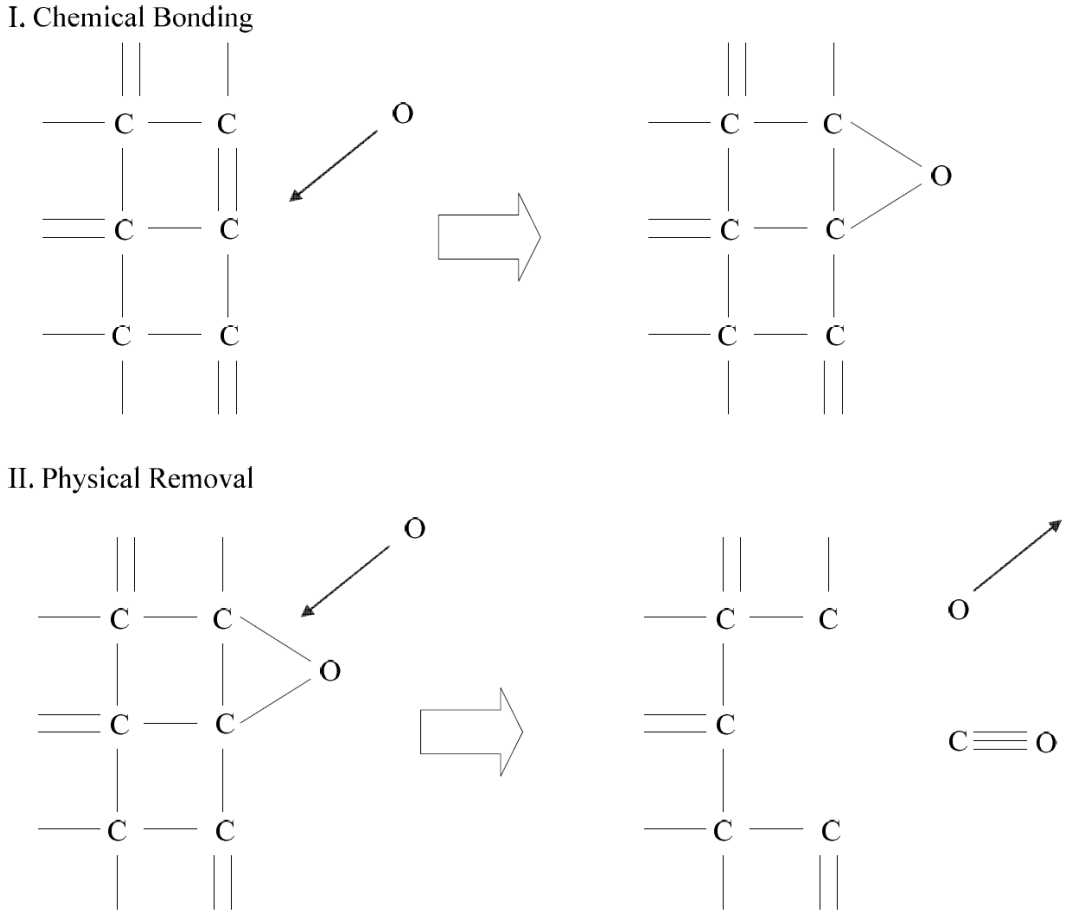

Figure 2. Atomic Oxygen Erosion of Example Graphite Surface [9]

After the erosion process, the example graphite structure is left with one fewer carbon atom. Thus, atomic oxygen can be said to be eroding the surface of a polymeric material one molecule at a time. The reaction efficiency of a material with atomic oxygen plays a large part in the material's erosion speed. The reaction efficiency is measured in volume loss per incident oxygen atom, cm^3/atom, and is also often referred to as the erosion rate. More information about the erosion rate can be found in Section 4.1.

When atomic oxygen erodes a surface, the remaining material is much rougher than before. This roughness can have an impact on the reflectivity of the material. The amount of surface roughening also depends on the energy of the incident atomic oxygen. On orbit, a spacecraft is flying through atomic oxygen at orbital speed, which in LEO can be around 7.5 km/sec. The atomic oxygen in this case has an energy of approximately 4.7 eV. However, atomic oxygen without orbital speed has no kinetic energy. It only has thermal energy, which is on the order of ~.01 eV [9]. If the incoming atomic oxygen is highly directional and at orbital speed, the eroded surface becomes extremely rough, with jagged rod and cone structures developing. These cones can have a depth of around 1 micrometer [10]. However, if the material is exposed to more isotropic, thermal speed atomic oxygen, the surface is left with relatively minor roughness, with feature sizes less than 0.1 micrometer [10]. The difference in the surface roughness can be seen in Figure 3. The left image shows the surface of a Kapton H sample that was returned from the Long Duration Exposure Facility (LDEF) mission. Visible in the picture are the extreme rods and cones that are characteristic of orbital energy atomic oxygen. The right image shows the surface of Kapton H when exposed to isotropic, thermal energy atomic oxygen in a ground-based facility. In this image, the top half represents Kapton H unexposed to

atomic oxygen. The exposed region is still visibly rougher, but the topography does not appear to be as drastic as in the left image. Both images were taken with a scanning electron microscope, though the scale used in the pictures is different.

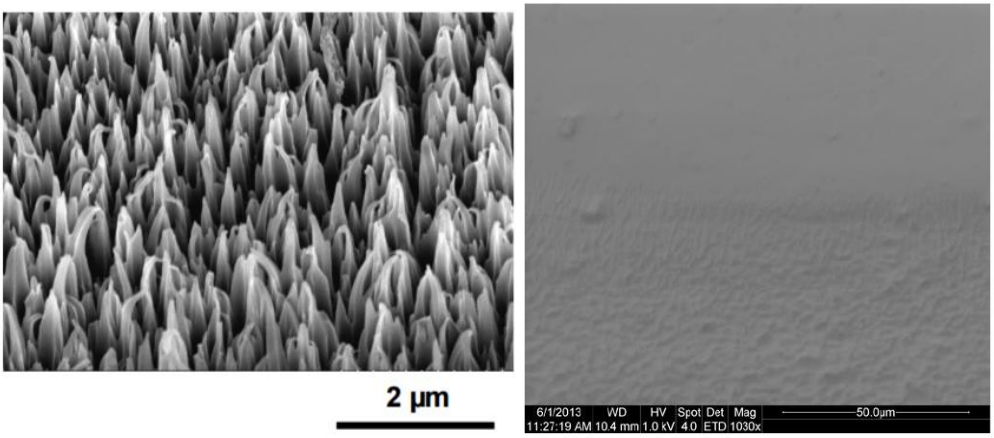

Figure 3. Surface Properties of Kapton H When Exposed to Orbital energy AO (left) and Thermal Energy AO (right) [11] [12]

To protect polymers from atomic oxygen erosion effects, metallic protective coatings are applied. Two of the most common coatings are silicon dioxide and aluminum. In both coatings, the incoming atomic oxygen creates an oxide layer on the top surface of the coating, which prevents any further reaction with the oxygen [11]. However, this does involve oxidation of the coating layer, which can change the optical properties of the material. Thus, one consideration for coating selection is how a change in optical properties will affect the function of the polymer [13]. For example, if the polymer was a multi-layer insulation (MLI) blanket, a decrease in reflectance of the coating means that the blanket might absorb more heat than initially desired.

The other major consideration in coating selection is the number of defects that can lead to undercutting. Undercutting occurs when atomic oxygen finds a defect in the coating and reacts with the polymer beneath. This can have severe consequences depending on the number of defects and whether the polymer is coated on both sides. For

example, if the polymer is thin and coated on both sides, any atomic oxygen that finds its way through a defect will become trapped inside the coatings. This leads to an even higher reaction efficiency with the material. But, if the polymer has a coating on only one side, the atomic oxygen erodes a crater at the site of the defect. Figure 4 illustrates these two cases. A Monte Carlo simulation with orbital energy atomic oxygen was used to predict the resulting erosion pattern of Kapton H. The figure shows that applying a protective coating on both sides of the material leads to higher mass loss than applying a coating on just one side.

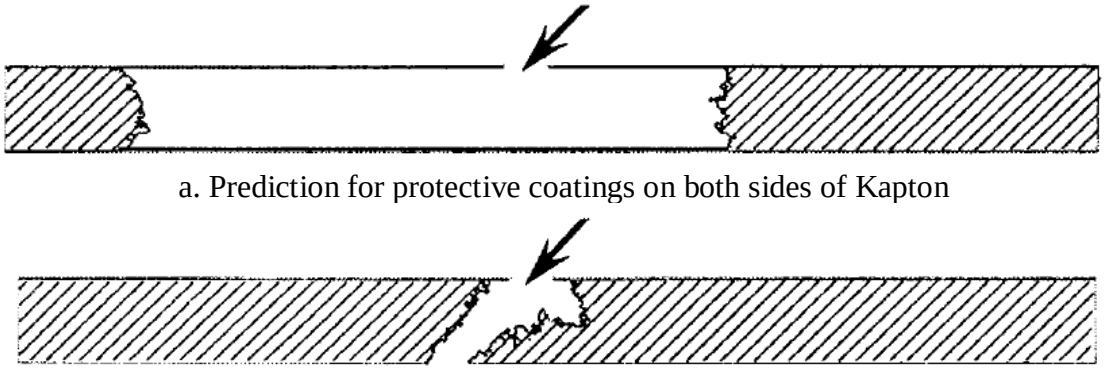

a. Prediction for protective coatings on both sides of Kapton

b. Prediction for protective coating on only one side of Kapton

Figure 4. Monte Carlo Simulation of Erosion for Aluminum Protected Kapton [14]

Even for a polymer coated on only one side, if the number of defects is sufficient, the atomic oxygen can create undercut cavities in the polymer, structurally compromising the material. Thus, it is important to minimize the number of defects in the atomic oxygen coating. For example, a vacuum-deposited aluminum coating typically has a larger defect density than sputter-deposited silicon dioxide [14]. If the number of defects is desired to be even further minimized, applying a surface level coating can reduce the defect density [11] .

Atomic oxygen effects have been thoroughly studied for thin film polymer materials in the context of mass loss and optical property changes relating to thermal considerations. However, the effect of atomic oxygen on a thin film polymer material has not yet been studied in the context of solar sailing. Solar sails will have different design considerations than the other applications involving polymer materials. So, if solar sails are to be used in LEO de-orbit missions, this gap in atomic oxygen knowledge must be filled.

2.0 Objective

The objective of this thesis is to determine the effect of atomic oxygen on a thin sheet of Mylar, aluminized on one side, that is used as solar sail material. The solar sail will be tested in the context of an example mission, a de-orbit sail that can be applied to a LEO satellite at 800 km in altitude to help the satellite de-orbit within 25 years. The atomic oxygen degradation will be split up into two categories: how it affects the survivability of the solar sail and how it affects the performance of the solar sail.

Survivability in this case means how long the solar sail material can be expected to last in an atomic oxygen environment. When the uncoated side of the material is exposed to atomic oxygen, the total amount of atomic oxygen needed to completely erode the Mylar will be estimated and experimentally verified. This represents a non-nominal mission where the uncoated side of the sail is exposed to atomic oxygen. With the coated side of the material exposed to atomic oxygen, the amount of undercutting will be determined by mass loss and surface topography measurements. This determines survivability of a nominal mission, where the aluminized side of the sail always faces the incoming atomic oxygen.

Performance in this example mission can be measured by how long it takes the solar sail to successfully de-orbit the satellite. With the coated side of the material exposed, the oxidation of the aluminum coating is expected to produce a change in the optical properties of the material. With a change in optical properties, the solar sail will generate less force and thus take a longer time to de-orbit the satellite. Therefore, the degradation of the performance of the sail will be the amount of time the satellite takes to

de-orbit without taking optical degradation into account versus the amount of time with optical degradation.

The overall goal of this paper is to understand the effect atomic oxygen has on a thin film polymer material in the context of using the material as a solar sail. The designers of future solar sail missions in LEO must take into consideration how atomic oxygen will degrade the sail material. If more LEO solar sail missions are developed, like the de-orbit sail, confidence in solar sailing technology will grow. Then, solar sails can be used in the costlier interplanetary missions where they would have the largest benefit.

3.0 Materials and Apparatus

3.1 Solar Sail Material

The solar sail material that will be tested was donated by Ecliptic Enterprises. The material is made up of Mylar aluminized on one side. It is reported that the Mylar is 4.6 µm thick [15]. Additionally, the material was measured to be around 5.3 µm thick total, which would make the aluminum coating around 0.7 µm deep. The same material is planned to be used in the Planetary Society's Lightsail-2, in a solar sail that measures 32 square meters [16]. There is also a set of stitches on the aluminized side of the material. These stiches are meant to prevent the propagation of any rips, which could be caused by deployment or debris impact. The stiches form a grid pattern, 0.5 inch by 0.5 inch, with one direction of the stitches lying flat on the surface and the other direction of stitches lying on top of the first set and glued to the surface, holding the first direction of stitches in place as well. The stitches are made of 67 denier polyester yarn [15]. The density of the Mylar was measured to be 1.79 ± .51 g/ cm^3. The common density of Mylar, 1.39 g/ cm^3, is within the measured error bounds [17]. Figure 5 shows the uncoated side of the material and the coated side of the material. The side with the aluminum coating is shinier than the side without. Therefore, the aluminized side will be the side facing the sun, because the higher reflectivity corresponds to a larger force generated for the sail, as explained in Section 4.2.

Figure 5. Left: Uncoated Side of LightSail Material. Right: Aluminized Side of Material, with Stitches

3.2 Test Chamber

The atomic oxygen chamber being used is a capacitively coupled plasma (CCP) system that creates atomic oxygen. This system was first developed at California Polytechnic State University by Aerospace graduate student Max Glicklin [9]. The atomic oxygen of this system has two main differences to atomic oxygen created on orbit. In a CCP system, the oxygen will have thermal energy, which will be around 0.04 -0.1 eV. Additionally, the oxygen will be isotropic while atomic oxygen on orbit is highly directional. As previously discussed, it is expected that the uncoated Mylar would have a rougher surface after exposure to atomic oxygen on orbit than in this chamber. However, it is also expected that the erosion yield of uncoated Mylar will be 1.09 times higher in the CCP system than on orbit [18]. But, on the coated side of the Mylar, the undercutting experienced is expected to result in 0.005 times less mass loss in space versus in the thermal energy system [19]. Thus, this thermal energy system will provide a large overestimate to the amount of mass loss from undercutting. The benefit of using a CCP system is that it will be able to generate high fluxes, allowing for accelerated testing [9].

The general schematic for the CCP system can be seen below. The system includes a radio frequency (RF) power source connected to an electrode inside the vacuum chamber. A dark space shield surrounds the electrode, which helps prevent plasma from forming behind the electrode and helps minimize secondary emissions. Another electrode inside the vacuum enclosure is connected to the ground. The atomic oxygen plasma is generated between the two electrodes.

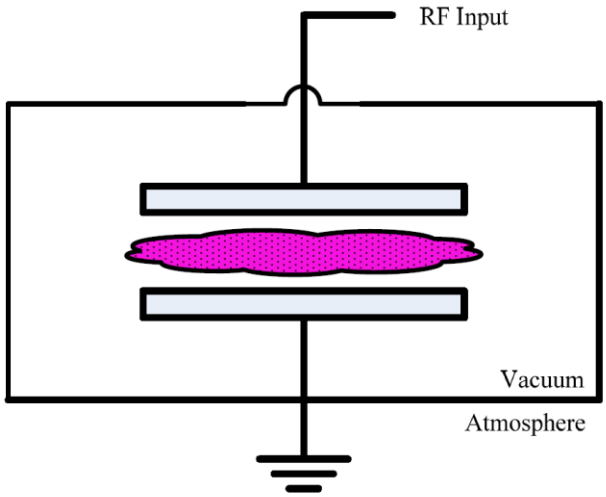

Figure 6. Capacitively Coupled Plasma System Schematic [9]

Powering the CCP in this system is a comprehensive power supply manufactured by Seren Industrial Power Systems. This system includes a Seren R301 MKII power generator that operates at 13.56 MHz. Attached is an AT3 matching network which is designed to match the impedance load of the plasma generator. This eliminates reflected signals produced in the load, protecting the RF generator from internal damage. Lastly, those systems are controlled by a Seren MC2 controller, which adjusts the variable capacitors inside the AT3 matchbox [9].

The vacuum chamber itself is a retrofitted Veeco Model 747 deposition chamber. It is a 50 cm diameter by 32 cm tall Pyrex cylinder, and has been modified to be airtight.

The chamber uses a Welch Model 1397 mechanical pump which is rated for ~500 liters/min pumping speed. The pump uses Welch DirecTorr Gold oil. There is also a gas insertion line into the chamber, controlled by a needle valve [9].

The RF electrode is a 6061-aluminum alloy disc that is 15.25 cm diameter and 0.9 cm thick. The RF power connector is attached to the electrode with a simple interference fit. The dark space shield encompasses the top electrode. There is small gap of 1.9 mm between the electrode itself and the dark space shield. The dark space shield and electrode are mounted to a hoist, to allow for easier access to the bottom plate. The bottom grounding plate is a 25.4 cm square aluminum plate. The gap distance between the electrode and the aluminum plate is set to 7.62 cm, which was determined to be optimal for generating atomic oxygen [9]. The aluminum plate has a small hole in the middle where the gas insertion line terminates. An aluminum cover plate with four evenly spaced holes is placed on top of the aluminum base plate for sample containment. Each hole has an identical radial and axial displacement from the RF electrode. It is through these holes that the atomic oxygen acts upon the test sample. The holes are 2.54 ± .003 cm in diameter, leading to an exposed area of 5.06 ± .02 cm^2. Both the dark space shield and the ground plate have Type 101 copper grounding straps. Figure 7 shows the vacuum chamber and RF power supply unit. More information about both the vacuum chamber and the RF power system can be found in Max Glicklin's thesis [9].

Figure 7. Atomic Oxygen Chamber (left) and RF Power Units (right)

4.0 Calculations

4.1 Atomic Oxygen

To determine how much atomic oxygen the sample is exposed to during a ground test, Kapton H is commonly used as a witness sample [20]. After measuring the mass loss from Kapton H, the effective fluence of atomic oxygen can be calculated with the following equation:

$$F = \frac{\Delta m_K}{A \rho_K E_K} \tag{1}$$

where F = effective fluence (atoms/cm^2), m = mass (grams), A = exposed area (cm^2), ρ = density (gram/cm^3), and E = erosion yield of witness material (cm^3/atom). Subscript "K" denotes Kapton.

In the above equation, the exposed area is the area of the holes cut out of the aluminum top plate, which is 5.06 ± .02 cm^2. The density of the Kapton H witness sample is 1.435 ± 0.002 g/cm^3 [9]. The proper erosion yield of Kapton H is determined by ASTM E 2089 to be 3.00 ± .07 x 10^{-24} cm^3/atom [20].

Sometimes, it is preferable to know the amount of atomic oxygen seen per second to compare between tests. The flux of atomic oxygen can be found from the fluence through the following equation:

$$f = \frac{F}{t} \tag{2}$$

where f = flux of atomic oxygen (atoms/cm^2/sec) and t = exposure time (sec).

To help determine survivability of the uncoated side of the test material, the amount of thickness loss will be measured. Once 4.6 µm of Mylar has been eroded, the sail will be lost because only the aluminum coating will remain. The thickness loss can be

estimated in two ways, using theoretical Mylar erosion values and using experimental mass loss values. To determine the theoretical mass loss, the following equation is used:

$$T_t = FE_M \tag{3}$$

where T_t = theoretical thickness loss (cm) and "M" denotes Mylar. Here, the erosion yield of uncoated Mylar is used, which is predicted to be 3.27 x 10^{-24} cm^3/atom for thermal energy systems [18].

This value will be compared to the experimental thickness loss, which is determined by the measured mass loss. Here the equation is:

$$T_e = \frac{\Delta m_M}{\rho_M A} \tag{4}$$

where T_e = experimental thickness loss (cm) and the density of the test Mylar is assumed to be the common value of 1.39 grams/cm^3.

4.2 Solar Sail Thrust

When photons from the sun hit the surface of a solar sail, there is a transfer of momentum to the sail which provides thrust to the sailcraft. This can be modeled as shown in Figure 8. The incoming light has a pressure *P* referred to as solar radiation pressure (SRP). The resulting pressure force can be split up into a normal component and a tangential component. The incidence angle defines the angle from sail normal to the incoming light.

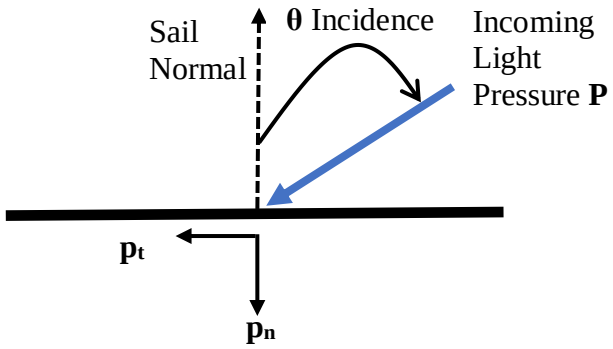

Figure 8. Light Pressure on Solar Sail

The resulting pressure terms can be calculated with the following equations. These equations are referred to as the nominal optics model [21].

$$p_n = P\left[(1+rs)\cos^2(\theta) + B_f(1-s)r\cos(\theta) + (1-r)\frac{\varepsilon_f B_f - \varepsilon_b B_b}{\varepsilon_f + \varepsilon_b}\cos(\theta)\right] \quad (5)$$

$$p_t = P[(1-rs)\cos(\theta)\sin(\theta)] \quad (6)$$

where p = resulting pressure force, with "n" for normal and "t" for tangential directions (μN/m^2), P = solar radiation pressure (μN/m^2), r = fraction of photons reflected, as opposed to absorbed, s = fraction thereof reflected specularly, ε = emissivity, with "f" for front side and "b" for back side, and B = Lambertian radiator coefficient.

At 1 AU from the sun, the value for P is 4.563 μN/m^2 [21]. Additionally, this can be assumed constant with solar activity, as the effect of solar activity on solar irradiance is minimal [22].

In the nominal optics model, there are six parameters specific to the material that need to be known: total reflection, specular reflection, front and back side emissivities, and front and back side Lambertian radiator coefficients. All six of these parameters could be degraded after exposure to atomic oxygen, so all of them would need to be measured before and after exposure.

To reduce the number of measured variables, a different model for solar sail force will be used. This model, termed the linear photonic thrust model, drops all terms with Lambertian radiator coefficients. This is shown in the equations below [21]:

$$p_n = (1 + rs)P\cos^2(\theta) \tag{7}$$

$$p_t = (1 - rs)P\cos(\theta)\sin(\theta) \tag{8}$$

Using the linear model reduces the number of measured material parameters from six to two. Additionally, in most cases this approximation results in similar values to the nominal optics model. It has been shown that with worst-case values for degradation and incidence angle, the error from this approximation only reaches about 10% [21]. Thus, because the linear thrust model reduces the number of measured variables while limiting the error introduced by the approximation, this model will be used for the rest of this thesis. When evaluating the performance of the solar sail, it will be important to measure how both the total reflectivity and specular reflectivity degrade once the material is exposed to atomic oxygen.

4.3 Average Reflectance Values

The reflectance values for a material often depend on the wavelength of the light being measured. The measuring device used, a Surface Optics 410 Solar Reflectometer loaned by SpaceX, gathers reflectance data in seven separate wavelength bins. However, equations (7) and (8) use one value of total and specular reflectance. So, to find the required values to use those equations, the measured reflectance data must be averaged together to form one value. If a simple average by wavelength is taken, the wavelength bins that are larger will have a bigger impact on the result. However, that can be misleading because the sun does not output all wavelengths evenly, so a larger

wavelength bin in an uncommon solar wavelength should still have a relatively small impact. Therefore, the most accurate method of determining the average reflectance value will be to take a weighted average with respect to the solar output. In this way, the more common wavelengths of light have the largest impact on the averaged reflectance value.

The spectral irradiance of the sun can be estimated by assuming that the sun is a blackbody. In this case, the flux of light from the sun can be found using Planck's law, shown below [23]:

$$I(\lambda) = \frac{2\pi hc^2}{\lambda^5\left(e^{\frac{hc}{k\lambda T}} - 1\right)} \tag{9}$$

where I = spectral irradiance (W/m^3), λ = wavelength of light (m), h = Plank's constant (Js), c = speed of light (m/s), k = Boltzmann's constant (J/K), and T = blackbody temperature (K). The sun's blackbody temperature can be estimated to be 5777 K [23].

Figure 9 shows the spectral irradiance of the sun calculated with equation (9).

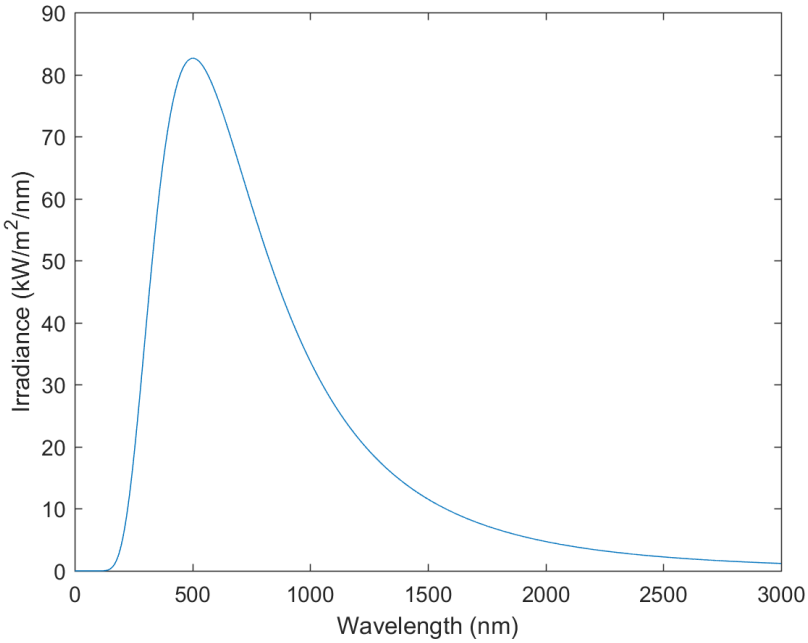

Figure 9. Spectral Irradiance for the Sun, T = 5777 K

It can be seen from Figure 9 that the sun has a maximum output at a wavelength around 500 nm, which is visible, green light. Therefore, the reflectance measurements taken for the visible spectrum will be the most influential. To find out what weight every wavelength bin should receive, the amount of solar flux over that wavelength bin will be compared to the total solar flux. This can be shown in the following equation:

$$w = \frac{\int_{\lambda_1}^{\lambda_2} I(\lambda)}{\int_0^{\infty} I(\lambda)} \tag{10}$$

where w = weight, and λ_1, λ_2 = lower and upper bounds of the wavelength bin.

The total integrated solar flux across all wavelengths can be found using the Stefan-Boltzmann law, shown below [23]:

$$\int_0^{\infty} I(\lambda) = \sigma T^4 \tag{11}$$

where σ = Stefan-Boltzmann constant ($W/m^2/K^4$).

Using the sun's temperature as 5777 K, the total flux from the sun reaches 6.316 $x10^4$ kW/m^2. Using this value in equation (11), as well as integrating equation (10) across the different wavelength bins, will determine the best weights for the different wavelength bins. The results are shown in Table 2:

Table 2. Weights for Average Reflectance Values

Wavelength Bin (nm)	Type	Weight
335-380	Ultraviolet	.0398
400-540	Visible	.1641
480-600	Visible	.1661
590-720	Visible	.1463
700-1100	Infrared	.2554
1000-1700	Infrared	.1773
1700-2500	Infrared	.0510

Even though the visible light reflectance bin has a relatively small size, it still makes up a large portion of the weight due to the sun's peak output being centered in green light. Meanwhile, the largest bin is the furthest in the infrared, but it has a small weight because the sun doesn't output nearly as much light in the infrared wavelengths. A weighted average with these results should give an accurate estimation for the singular reflectance values to be used in equations (7) and (8).

4.4 Wrinkle Factor

The amount of specular reflection a surface produces is influenced by the smoothness of the surface. A surface with many wrinkles on it will have a different overall specular reflection than a perfectly smooth surface. This will become a problem when trying to analyze the data. If the sail samples used for control have a different number of wrinkles than the samples exposed to atomic oxygen, it will be impossible to tell how much the specular reflectivity changed due to the exposure. Thus, a method of predetermining the wrinkle level of a sample is needed, so that only samples with a

similar wrinkle level get compared. This wrinkle level is estimated with a wrinkle factor algorithm, created for the purposes of this thesis.

The first step in determining wrinkle level is to detect edges in a picture of the sample with an image processing algorithm. This allows the wrinkles to be distinguished from the rest of the sample. A Hessian-based multiscale image filtering algorithm has already been developed [24] and implemented into Matlab [25]. This Matlab algorithm is used to process an image of every sail sample to be used in this research. The results of the processing are shown below.

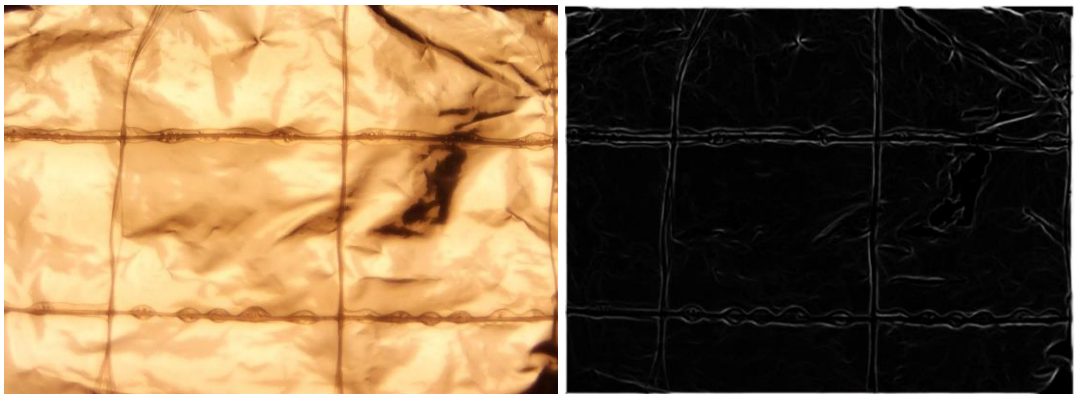

Figure 10. Sail Sample Edge Detection. Left- Image Before Processing. Right- Image After Processing

The edge detection program did find most of the wrinkles in the material, however, it also found all the stitches in the material as well. While this isn't ideal, it does not completely inhibit the algorithm from providing useful data.

To calculate wrinkle factor, the number of white pixels is divided by the total number of pixels in the picture. This gives a rough estimation of the wrinkle percentage of the sample. For example, the sample in Figure 10 has a wrinkle factor of 0.1, meaning roughly 10% of the material was covered in either wrinkles or stitches. Figure 11 shows how the algorithm measured a sample that was heavily wrinkled.

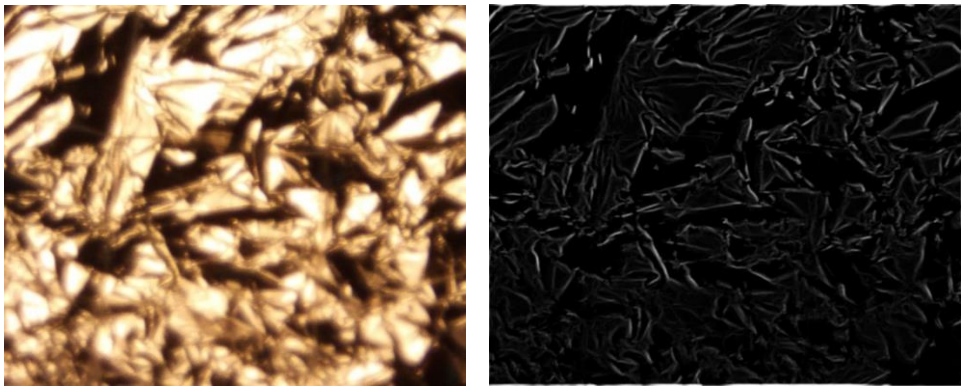

Figure 11. Heavily Wrinkled Edge Detection. Left- Image Before Processing. Right- Image After Processing

In this image, the edge detector appears to have found most of the wrinkles and a few of the stitches. But, it did not find all the stitches, which is why it is difficult to account for the stitches in the wrinkle factor calculation. So, due to the stitches, this method does not produce a completely accurate wrinkle factor. However, because all the samples will have a similar amount of stitches in the picture, this method should be able to give a good approximation for the wrinkle factor. Showing this, the calculated wrinkle factor for Figure 11 is 0.33, significantly higher than Figure 10. While the inclusion of the stiches in Figure 10 isn't ideal, the large wrinkle factor difference between it and Figure 11 shows that a satisfactory numerical comparison can be made between lightly wrinkled samples and heavily wrinkled samples. Figure 12 is generated when the wrinkle factor is calculated for 90 different sail samples.

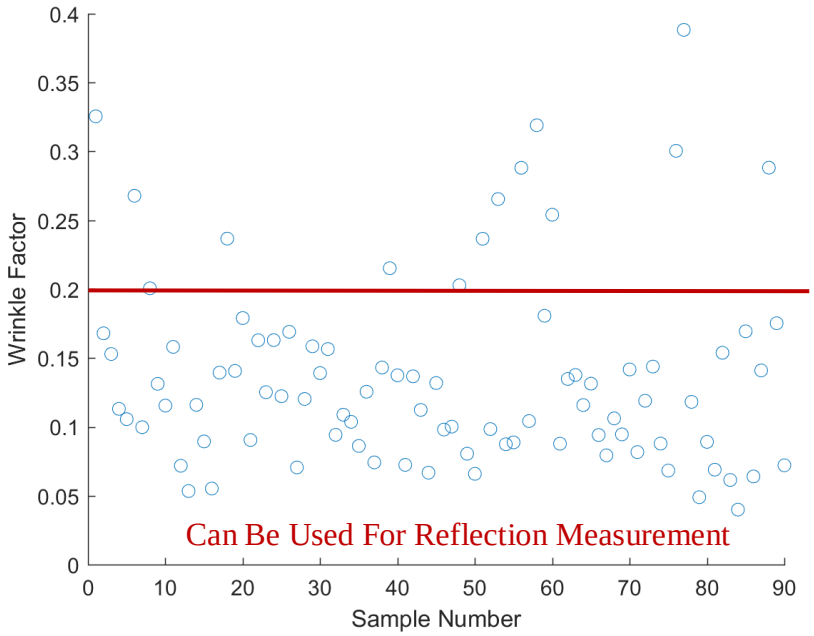

Figure 12. Wrinkle Factor of 90 Sail Samples

From visual comparison of unprocessed images, the samples with a wrinkle factor less than 0.2 look to have a similar wrinkle level. The wrinkle data in Figure 12 shows that the average wrinkle factor is 0.13± .07, with only heavily wrinkled outliers outside the one standard deviation range. Therefore, only samples with a wrinkle factor less than 0.2 will be chosen to be analyzed for a change in reflection properties after exposure to atomic oxygen. All control samples will come from this range as well. While this method will not be able to perfectly account for the amount of wrinkles a sample has and what the change on specular reflectivity may be, this method will at least pre-emptively determine which samples shouldn't be included in reflectance measurements, because the wrinkle level will certainly overshadow any potential change from atomic oxygen.

5.0 Orbital Analysis

5.1 Orbital Analysis

The total time until sailcraft de-orbit will be used to determine the performance of the sailcraft. To do this, first the orbital equations of motion must be understood. It is assumed that the sailcraft is in a 2-body 2D orbit around the Earth, with drag and solar radiation pressure as the only perturbing forces. Because the sailcraft is trying to de-orbit, the semi-major axis of the orbit is the main parameter of interest. Therefore, a 2D orbit can be assumed without significantly impacting the de-orbit results. This helps simplify the calculations. For example, normally in LEO, the non-spherical Earth perturbation is included in orbital calculations because it creates a larger force than drag and SRP. However, the non-spherical Earth perturbation predominantly changes the right ascension and argument of perigee of the orbit while not affecting the semi-major axis [26]. Therefore, it does not need to be considered in the 2D case.

The equations of motion will be set up in an Earth-centered inertial reference frame. Additionally, the position of the sun will be set to the positive y-axis, so that the SRP force always acts in the negative y-direction. $\vec{r}$ is used to define the position vector of the spacecraft. This setup can be seen in Figure 13.

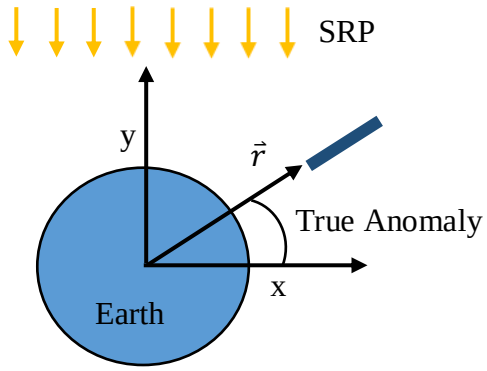

Figure 13. Earth Centered Inertial (ECI) Frame

The equations of motion for the sailcraft turn into the following [26]:

$$\vec{a} = -\frac{\mu}{r^3}\vec{r} + \vec{a}_{SRP} + \vec{a}_{Drag} \tag{12}$$

where $\vec{a}$ = total acceleration (N), and μ = gravitational acceleration parameter of the Earth, defined to be 3.986 x 10^{14} (m^3/s^2).

The acceleration due to solar radiation pressure can be found by multiplying the value in equations (7) and (8) by the ballistic coefficient of the sailcraft:

$$\vec{a}_{SRP} = BC(\vec{p}_n + \vec{p}_t) \tag{13}$$

where *BC* = ballistic coefficient, defined as area of solar sail divided by mass of spacecraft (m^2/kg), and $\vec{p}$ = resultant solar radiation pressure with magnitude as defined by equations (7) and (8), and direction defined in the ECI coordinate frame.

The acceleration due to drag is defined by the following equation [26]:

$$\vec{a}_{Drag} = \frac{-BC}{2} C_d \rho v_{rel} \vec{v}_{rel}\cos(\alpha) \tag{14}$$

where C_d = coefficient of drag, ρ = density of air (kg/m^3), α = drag incidence angle. v_{rel} = the magnitude of $\vec{v}_{rel}$ (m/s), where $\vec{v}_{rel}$ = velocity of sailcraft relative to atmosphere, defined below for the frame of reference in Figure 13:

$$\vec{v}_{rel} = \frac{\vec{v}}{v}\left[v - rw_e\cos(i)\right] \tag{15}$$

with $\vec{v}$ = velocity vector of sailcraft (m/s), v = magnitude of the velocity vector (m/s), w_e = angular velocity of Earth about its own axis, defined as 72.9211 x 10^{-6} (rad/s), i = inclination of orbit, and r = magnitude of the position vector (m).

For this analysis, the area presented to drag and solar radiation pressure will be assumed to be entirely from the solar sail. Therefore, the coefficient of drag for the sailcraft will be assumed to be both constant and equal to that of a flat perpendicular plate, which is 1.28 [27]. It is also important to note that, traditionally, equation (14) is written in terms of the area exposed to drag, instead of the total area of the spacecraft. However, because the solar sail is assumed to make up the entire area of the spacecraft, the exposed area can be written instead in terms of the total area multiplied by an incidence angle term. The incidence angle term is the *cos(α)* term in equation (14). This substitution allows both equation (13) and equation (14) to be written in terms of the same ballistic coefficient, which will be helpful for future calculations.

The model NRLMSISE-00 will be used to calculate both atmospheric density and atomic oxygen density at a certain altitude. To use this model, the solar activity must be defined in terms of a daily F10.7 value, the F10.7 value over an 81-day average, and the magnetic index A_p. This analysis will examine three different levels of solar activity, as defined in Table 3. These values were determined by looking at historical data for F10.7 and A_p indices [28].

Table 3. Solar Activity Threshold Values

Name	F10.7: Daily	F10.7: 81 day	Magnetic Index: A_p
Low Solar Activity	80	80	8
Medium Solar Activity	120	120	12
High Solar Activity	160	160	16

5.2 Drag Versus Solar Radiation Pressure

A common concern for solar sails in LEO is that the drag force will overshadow the effect of solar radiation pressure, making the solar sail more akin to a parachute than a sail [8]. However, this does not apply for orbits of all altitudes. The density of air, and therefore the drag force, decrease exponentially with altitude, while the solar radiation pressure force will remain constant. At some altitude the magnitude of these forces will be equal. This altitude can be found by taking the ratio between the magnitude of equation (14) over the magnitude of equation (13). The ballistic coefficient in these equations will divide out, so the ratio is not impacted by spacecraft-specific parameters. Figure 14 shows how the ratio changes with respect to altitude. Additional assumptions made to create the figure include circular orbit, zero inclination, r=s=1, and the incidence angle for both drag and SRP is zero. When the incidence angle is zero, the area exposed to both drag and SRP is the same. Therefore, this ratio is comparing the maximum magnitudes of both forces. When the ratio value is above 1, the drag force is larger than the SRP force. When the ratio is below 1, the opposite is true.

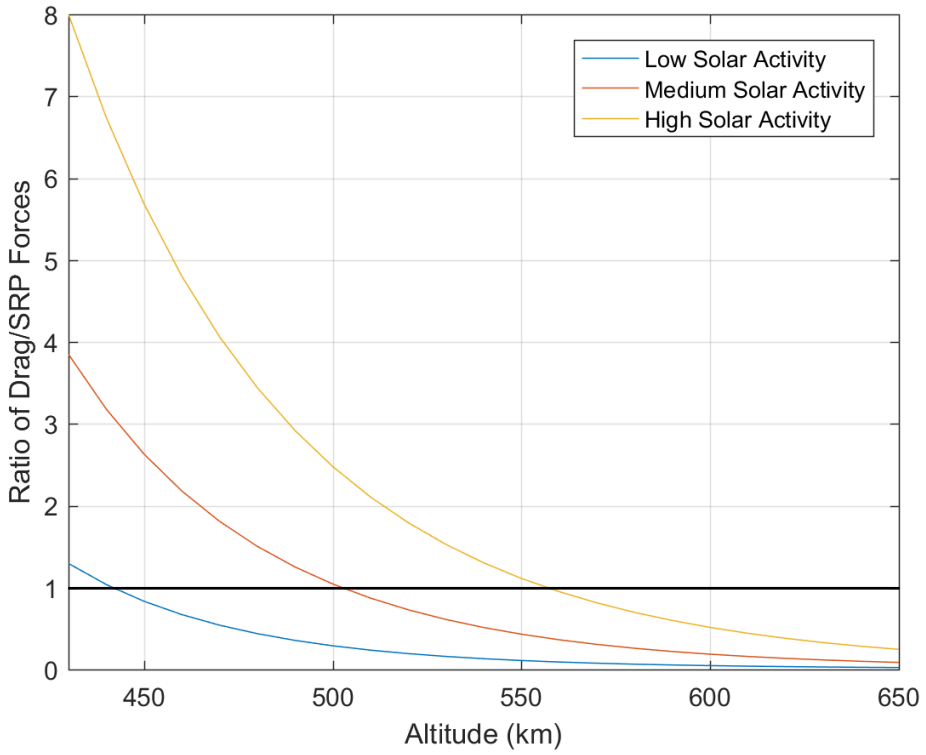

Figure 14. Comparison of Drag and SRP Forces

The altitude where the magnitudes of drag and SRP are equal is approximately 450 km during low solar activity, 500 km during medium solar activity, and 550 km during high solar activity. Therefore, a solar sail is better off being used as a drag device below about 500 km. Above 500 km, a solar sail will generate a similar or larger force on the satellite than drag. A solar sail is then a beneficial de-orbiting device in orbits above 500 km, which is a common range for LEO satellites. For example, most sun-synchronous orbit possibilities are found above that height [26].

For the duration of the thesis, trajectories above 500 km during medium solar activity will be said to be in the SRP dominant region, while trajectories below 500 km will be in the drag-dominant region. The boundary value will change depending on the solar activity level being examined.

5.3 Optimal De-Orbit Trajectory

While the previous section assumed an incidence angle of zero for both drag and SRP, this is rarely the case during a real orbit. Thus, when evaluating the de-orbit time of an example sailcraft, it is necessary to know how the sail will be pointing so that the true incidence angle can be calculated. Unfortunately, a definitive algorithm to determine the best sail pointing angle was not available in research articles. Therefore, one will be created for the orbital situation described in this paper.

As discussed in section 5.1, there are three forces acting on the solar sail: gravity, SRP, and drag. Both the SRP and drag forces are dependent upon the sail pointing angle. In the case of drag, as seen in equation (14), only the magnitude of the drag force is affected by the sail pointing angle, due to the $cos(\alpha)$ term. The direction of drag will always be in the opposite velocity vector direction, independent of the sail pointing angle. However, in the SRP equations (7) and (8), both magnitude and direction are dependent upon the sail pointing angle. Direction is affected because the primary resultant force is in the direction opposite the sail normal vector, and magnitude is affected because of the $cos^2(\theta)$ term in the equations.

In most optimization problems, a derivative must be taken. However, the derivatives of the equations of motion in this situation become difficult to handle analytically, due to the multiple directions and angles involved. So, for the scope of this work, a simpler approach will be taken. To determine the optimal sail pointing angle to raise an orbit, the sail angle that maximizes the force in the velocity vector direction is found at every time step [29]. So, to lower an orbit, maximizing force in the opposite velocity vector at every time step should provide the optimal sail angle to de-orbit over the entire trajectory.

A code was created that integrates the equation of motion in equation (12) using Matlab's ode45 function [30]. At every time step of the integrator, a new value for drag force maximum magnitude was found. Then, a Nelder-Mead simplex algorithm, as implemented in Matlab's fminsearch function, finds the sail pointing angle that maximizes the force from both drag and SRP in the opposite velocity vector direction [31]. The sail angle was defined as the angle between the sail normal direction and the sail velocity vector direction. The sail angle is positive if the normal vector is right of the velocity vector, and negative if the normal vector is left of the velocity vector. This is further illustrated in Figure 15. Additionally, the sail angle was never allowed to have an absolute value greater than 90 degrees. This would indicate that the back, uncoated side of the solar sail is in the velocity vector direction. As section 7.1 explains, in nominal operation the uncoated side of a solar sail should experience minimum atomic oxygen exposure throughout the trajectory.

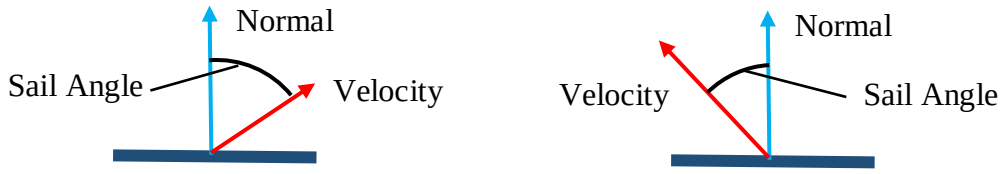

Figure 15. Sail Angle Definition. Left- Negative Angle, Right- Positive Angle

To test that the code was working as intended, it was applied to a few example problems. In these problems, the sail was assumed to be perfectly reflecting, meaning that in equations (7) and (8) r = s = 1. This makes the tangential force disappear, so that the only force generated by the solar sail is in the negative normal direction. For the first two example problems, only one orbit of the sailcraft is examined. True anomaly represents the angle the sailcraft makes with the positive x-axis, as defined in Figure 13.

In the first example problem, the SRP force is removed, so only drag is being experienced. It is expected that the algorithm will choose a sail angle of 0 every time, to indicate maximum area in the velocity vector direction. Figure 16 shows the algorithm's result.

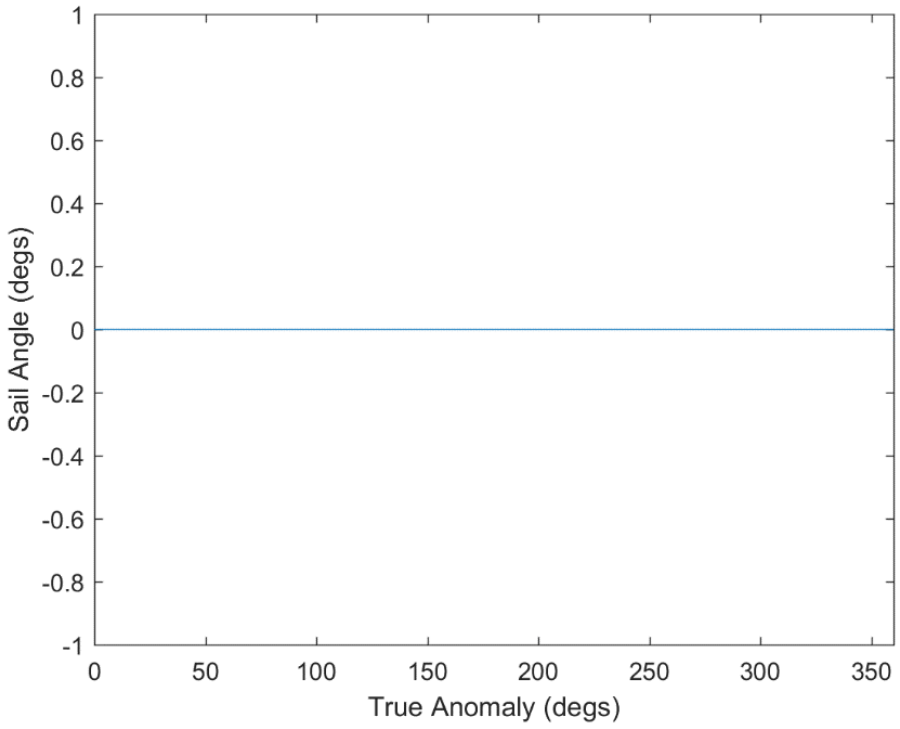

Figure 16. Optimal Sail Angle: Drag-Only Case

The result of 0 degrees in sail pointing angle means the algorithm correctly determined that the best sail normal direction is the same as the velocity direction at every time step. Having been shown to work in a drag-only case, the next example is with only SRP acting on the sailcraft, while drag is set to zero. To validate this, consideration must be taken as to what the result should look like. The below figure demonstrates the optimal sail angle at different positions in the 2D orbit.

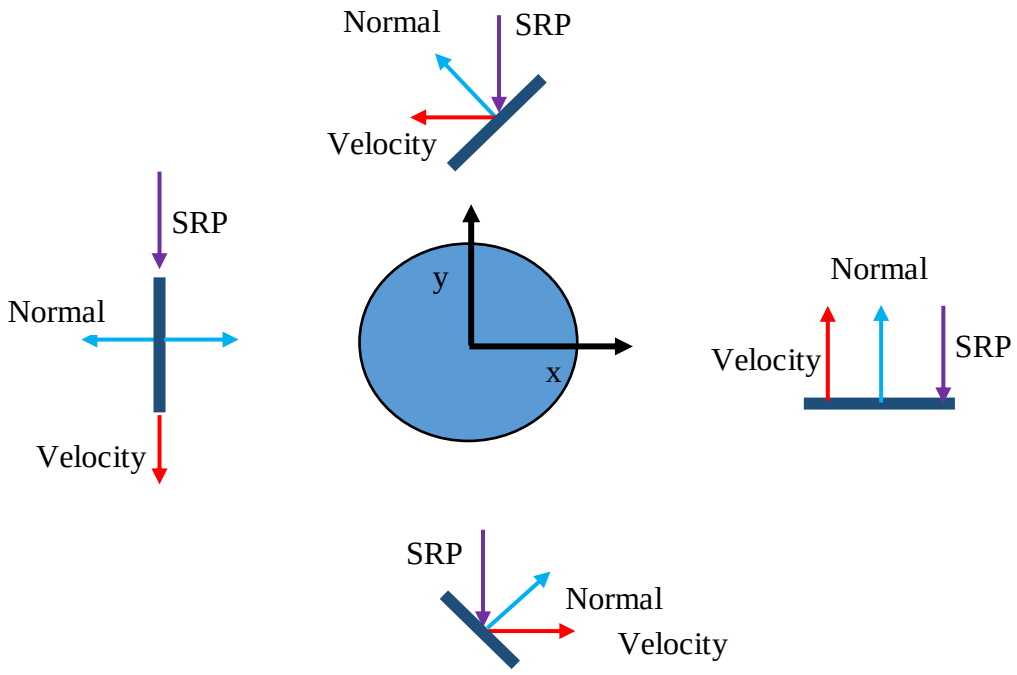

Figure 17. Optimal Sail Angle to De-Orbit with SRP

When the sail is on the positive x-axis, facing upwards maximizes the solar radiation pressure on the sail while also creating the resultant sail force in the exact opposite direction of velocity. On the positive y-axis, the sail should be at approximately a 45-degree angle, to maximize area exposed to solar radiation while also ensuring that the thrust generated acts mostly opposite the velocity vector direction. Here the sail angle should be positive, indicating that the normal vector is to the right of the velocity vector. On the negative y-axis, the same is true; however, the sail angle will now be negative, indicating that the normal vector is left of the velocity vector. On the negative x-axis, the sail angle should be ±90 degrees, as in this position any other angle would generate force in the velocity vector direction. So, the sail angle slowly increases to 90 during the first half of the trajectory, then flips around completely to increase from -90 to zero for the

second half of the trajectory. Figure 18 shows the results of the algorithm for the SRP only example.

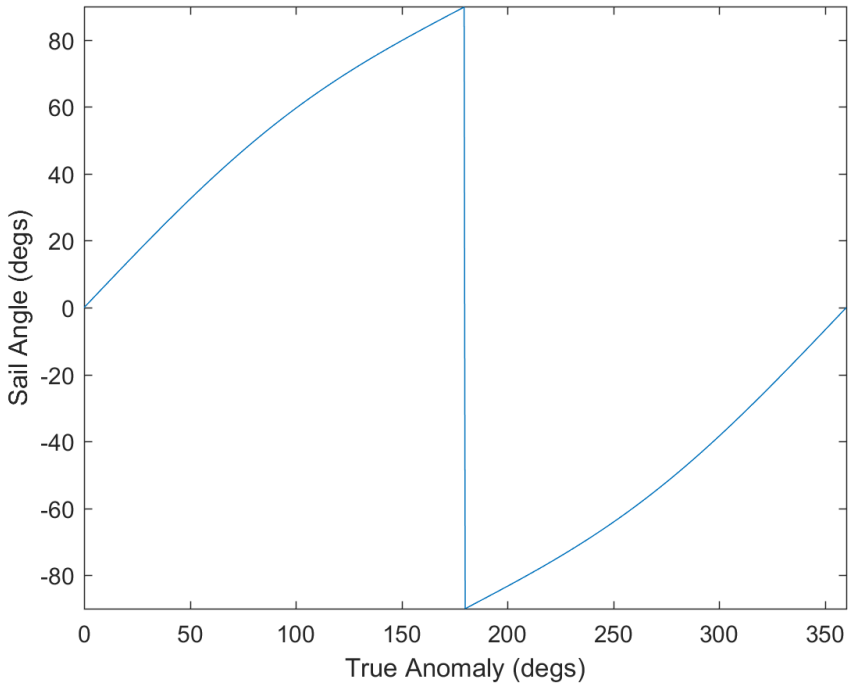

Figure 18. Optimal Sail Angle: SRP-Only Case

Because the sail angle output by the algorithm matches the sail angle prediction in Figure 17, the algorithm is verified to work with solar radiation pressure. It is important to note that the instantaneous 180-degree rotation of the sail is not practical for any real sail. However, this optimization is being developed to better understand the performance loss of a theoretical sailcraft. Developing a realistic control law for the sail that follows the results of this optimization is outside of the scope of this thesis.

The last example problem looks at the entire de-orbit trajectory of a satellite. For this test case, the ballistic coefficient was assumed to be 250, to produce a quick de-orbit time. The initial orbit was set to circular at 800 km, and the solar activity was assumed medium, following the definitions in Table 3. Inclination in this test case is assumed to be

zero. Lastly, the effect of Earth's shadowing will be included. While the sail is in Earth's penumbra, no SRP force exists, so the sail angle will jump to zero to maximize the drag force. The shadowing equations used are from the author Curtis [26].

This test case highlights the interactions between drag and SRP. When the sail first starts out in the 800-km orbit, the sail angle should resemble that shown in Figure 18, as the satellite is the SRP-dominated region. However, as the altitude of the spacecraft decreases and drag starts to become the dominant force, the sail angle should stay closer to zero. Figure 19 below shows the sail angle throughout the entire trajectory.

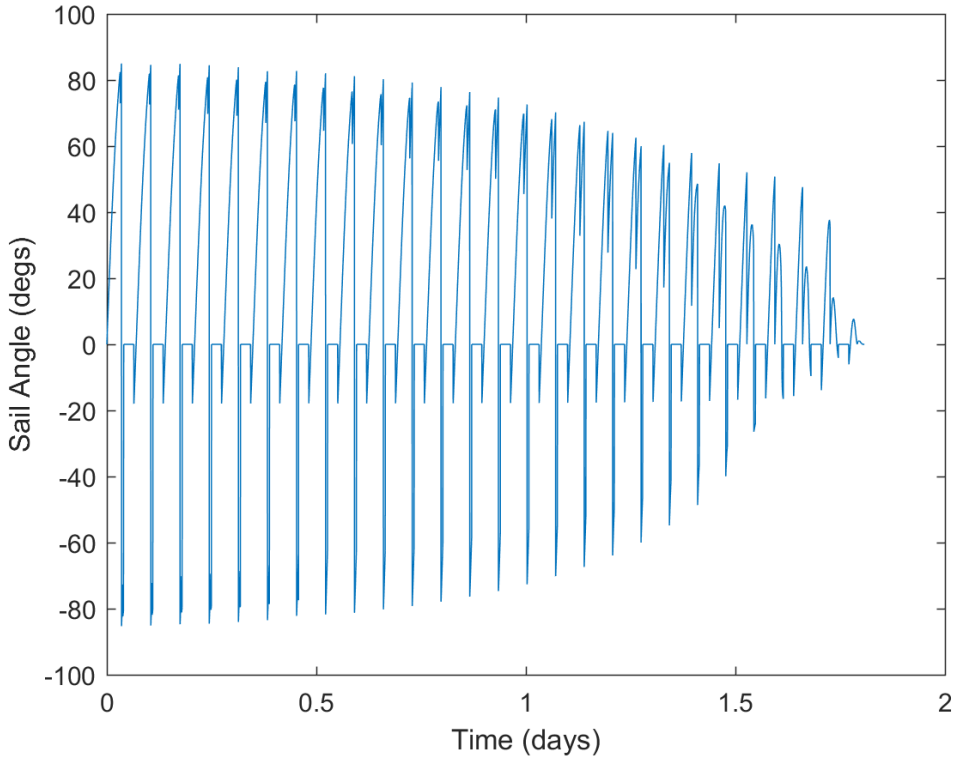

Figure 19. Sail Angle for Solar Sail: BC = 250, r=s=1

Just as predicted, the sail angle starts by oscillating between ± 90 degrees, just like in the SRP only test case. However, as the sail de-orbits, the peak of the curves appears lower and lower, as the velocity vector direction becomes the new preferred

direction for the sail. The flat lines between every curve represent the areas where the solar sail is in Earth's shadow, so the algorithm correctly predicted the best sail angle to be 0 degrees. Figure 20 depicts the altitude of the spacecraft alongside the total atomic oxygen fluence experienced.

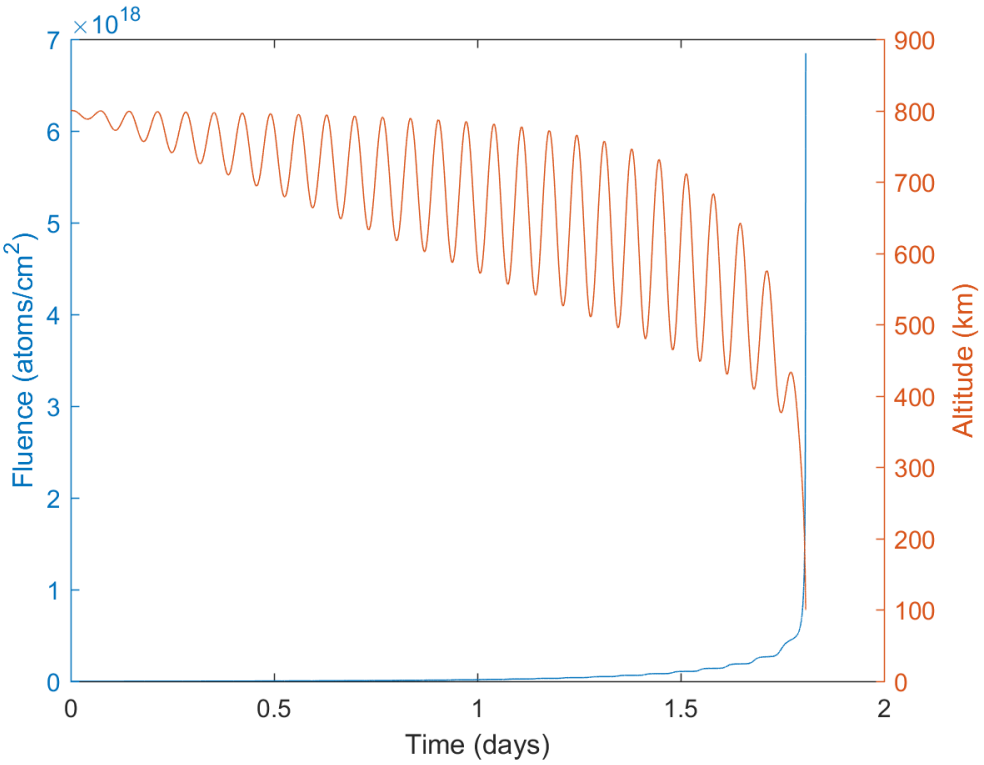

Figure 20. Altitude and Total AO Fluence for Solar Sail: BC = 250, r=s=1

The spacecraft started in a circular orbit; however, the periodicity of the altitude shows that the orbit quickly becomes eccentric. This is because the largest acceleration gain during the SRP-dominated region is when the spacecraft is close to the positive x-axis, while little to no acceleration is experienced while the spacecraft is close to the negative x-axis. Thus, the perigee of the orbit becomes the negative x-axis side, and apogee occurs on the positive x-axis. Every time the spacecraft flies through apogee, the maximum acceleration region, the perigee drops lower. Eventually, as perigee drops to below 500 km, drag becomes the dominant force. Then the region of maximum

acceleration starts to occur during perigee. After this point, the apogee of the orbit starts to drop as drag decreases it. Then the orbit quickly degenerates to 100 km, where it is said to re-enter. That is why in Figure 20, the apogee of the orbit seems to remain constant, while perigee continuously drops. But, after around 1.2 days, the perigee reaches 500 km and the apogee starts to fall as well.

The accumulated atomic oxygen fluence is also shown in Figure 20. The exponential growth of the atomic oxygen fluence can be explained through Figure 1. When the satellite is at a high altitude, Figure 1 shows that the number density of atomic oxygen is small. Therefore, the flux of atomic oxygen is small, so the fluence remains low. But, as the altitude of the satellite drops, the number density of atomic oxygen starts to increase exponentially. This correlates to large increases in both the flux and accumulated fluence values. Specifically, in Figure 20, it seems the fluence starts to experience significant increases around the time that apogee starts to decline. This is due to the satellite spending more total time in lower altitudes once apogee starts degrading.

The algorithm seems to have given the correct results for all simplified example problems, so it is considered verified and ready to be used in conjunction with the experimental data on optical degradation.

6.0 Tests Performed

All sail samples and Kapton witness samples were placed inside a separate vacuum to outgas before being tested inside the atomic oxygen vacuum chamber. This vacuum chamber kept the test material at a of pressure ~5 mTorr at room temperature for 24 hours, as recommended by ASTM E 2089 [20]. After 24 hours, the test materials were weighed and placed inside the atomic oxygen chamber within 10 minutes. By doing this, all mass loss seen after the atomic oxygen chamber can be said to be loss due to the atomic oxygen exposure, not outgassing. Tests 1 and 2, however, broke the 10-minute mark for time spent out of vacuum. In these tests, the Mylar was to be weighed more precisely, so a different scale was used. The samples ended up spending around 30 minutes out of vacuum before being placed inside the atomic oxygen chamber. Most of this time was spent walking to and from a different building with a more precise scale, while the samples were enclosed in a cardboard box. This more precise instrument was a Mettler-Toledo XS3DU scale with a readability of 0.001 mg. The high accuracy was needed for the mass measurements being taken on the Mylar, as discussed in Section 7.1.

The chamber pressure during the atomic oxygen test needed to be kept at 175 ± 10 mTorr during the duration of the test. The RF power generator was set to output at 125 W. These procedures are used to best produce an atomic oxygen plasma in accordance with the standard for thermal energy systems [9]. During the test, the chamber was monitored to ensure that the pressure remained in the desired range and that the reflected power remained zero. For the first few hours of a test, the chamber pressure and reflected power were monitored carefully, as they were most likely to change during this time.

The Kapton samples were weighed before and after every test. At every weighing, four different measurements were taken. The average value of these measurements became the nominal value, while the standard deviation of the measurements became the error bar. The fluence and flux values were found after every test by using equations (1) and (2). The below table reports the fluence and flux values for every test.

Table 4. Test Data Fluence And Flux

Test Number	Exposure Time (hours)	Effective Fluence ($atoms/cm^2$)	Effective Flux ($atoms/cm^2/s$)
1	3	$2.27 \pm .24 \times 10^{20}$	$2.10 \pm .22 \times 10^{16}$
2	1.5	$1.22 \pm .78 \times 10^{20}$	$2.27 \pm 1.45 \times 10^{16}$
3	11.73	$5.05 \pm 1.76 \times 10^{20}$	$1.20 \pm .42 \times 10^{16}$
4	7.25	$4.13 \pm 1.73 \times 10^{20}$	$1.58 \pm .66 \times 10^{16}$
5	16	$8.26 \pm 1.85 \times 10^{20}$	$1.43 \pm .32 \times 10^{16}$
6	23.6	$1.19 \pm .18 \times 10^{21}$	$1.40 \pm .21 \times 10^{16}$
7	23.7	$1.19 \pm .17 \times 10^{21}$	$1.40 \pm .20 \times 10^{16}$
8	21.75	$1.15 \pm .14 \times 10^{21}$	$1.47 \pm .18 \times 10^{16}$
9	8	$4.13 \pm 1.84 \times 10^{20}$	$1.43 \pm .64x\ 10^{16}$
10	10.5	$6.31 \pm 1.90 \times 10^{20}$	$1.67 \pm .50 \times 10^{16}$
11	16.75	$9.30 \pm 1.59 \times 10^{20}$	$1.54 \pm .26 \times 10^{16}$
12	12	$5.74 \pm 2.73 \times 10^{20}$	$1.32 \pm .62 \times 10^{16}$

The flux values in tests 3-12 are all within the error bounds of predicted flux values for this chamber, initially estimated to be around 1.6-1.8 x 10^{16} $atoms/cm^2$ during the creation of the chamber [9]. However, in the two shorter duration tests, the flux values were significantly larger. The chamber has a higher flux in the first couple hours of operation before settling down to a more constant value. This is likely due to the system not yet being in equilibrium, as the chamber's temperature starts to rise once the

RF energy is turned on. This temperature increase creates a pressure increase, which can cause the matching network to change parameters in the RF energy output. This state of non-equilibrium is also why the chamber needed to be monitored closely during this time.

Throughout all of the tests, the Kapton samples had a static charge that produced a variation of approximately 0.002 g in the mass measurements. This charge was likely accumulated while the material was in the atomic oxygen plasma. A good mitigation technique for the static charge was never determined. For the most part, the fluence and flux error bars were small relative to the nominal value. However, this was not true for test two. Here, the short duration of the test, combined with the inaccuracies in the mass measurements, led to a relatively large error bar for fluence and flux. If more tests were to be run in this atomic oxygen chamber for a short duration, it would be important to mitigate the static charge problem with the Kapton. Thankfully, for the purposes of this thesis, the high error bar on the second test's fluence does not have a significant impact on the results, as described in the next section.

7.0 Results

7.1 Survivability – Uncoated Side

To determine the survivability of the solar sail in withstanding atomic oxygen, the uncoated side of the solar sail is first examined. Using equation (3), and assuming that the Mylar portion of the solar sail is 4.6 µm thick, the sample should theoretically survive a fluence of up to 1.41 ± .04 $x10^{20}$ atoms/cm^2. After that, the Mylar should be completely eroded away, leaving only the aluminum coating. Experimentally, this fluence survivability was tested.

Test 1 in Table 4 test lasted three hours. It had a fluence larger than the theoretical survival limit, about 2.27 ± .24 $x10^{20}$ atoms/cm^2. Figure 21 shows what the Mylar looked like while in the test stand immediately before and after atomic oxygen exposure.

Figure 21. Uncoated Side- Before and After Exposure, Fluence ~ 2.27 $x10^{20}$

The material looks stressed, wrinkled, and shinier after exposure. Also, the stitches from the opposite side of the sample are visible, while they weren't beforehand. This indicates that the aluminum coating is primarily what is being observed, while the Mylar has disappeared.

To confirm that the Mylar had disappeared, mass loss measurements were taken of the sample before and after exposure. Equation (4) is used alongside the mass change in the material to estimate the thickness loss in the material. Table 5 below shows the results. Similar to the Kapton, four mass measurements were taken of each sample, and the standard deviation of the measurements became the error bar.

Table 5. Thickness Loss of Uncoated Sample, Fluence ~ 2.27 x10^{20}

Sample	Low End Loss (µm)	Nominal Loss (µm)	High End Loss (µm)
1	4.66	4.68	4.70
2	4.73	4.76	4.78
3	4.56	4.58	4.60

In all three samples, the error bar for the thickness loss is either on or above the known total thickness of the material. This means the chamber fluence was large enough to completely erode the Mylar.

After being measured, the remaining material in the exposure area soon disintegrated from the handling. Figure 22 shows what this deterioration looked like.

Figure 22. Uncoated Side- After Removal from Chamber, Fluence~2.27 x10^{20}

The sole portion of the sail left was the stiches. Because the Mylar makes up the structure of the film; the aluminum cannot keep itself together on its own. So, once the Mylar is gone, any small disturbance on the leftover aluminum coating causes it to fall apart. From both visual observation and mass loss measurements, the uncoated side of the Mylar cannot survive a fluence value of 2.27 $x10^{20}$ atoms/cm^3, agreeing with the theoretical measurements.

Test 2 in Table 4 lasted 1.5 hours in the chamber. This time, the Kapton witness samples measured a fluence of 1.22 ± 1.1 $x10^{20}$ atoms/cm^2. This is below the theoretical limit, so the Mylar should have survived.

Visually, some Mylar in the samples was left intact. Figure 23 shows what the samples looked like while they were still in the chamber, and once they were removed from the test stand. Instead of looking shiny like the pure aluminum coating in Figure 21, the samples show a discoloration. This is indicative of Mylar that has been exposed to atomic oxygen [32]. Additionally, the samples survived being taken out of the chamber, showing that the samples still have some structural integrity.

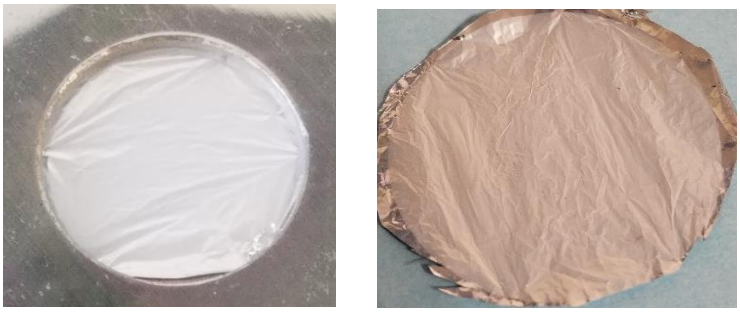

Figure 23. Uncoated Side- In Chamber and After Removal, Fluence ~ 1.22 $x10^{20}$

Table 6 shows the low end and high end thickness loss based on the measured mass loss. This time, the known thickness for the material, 4.6 µm, does not fall within

the error bars of the thickness loss. Therefore, the Mylar part of the sail survived this atomic oxygen exposure.

Table 6. Thickness Loss of Uncoated Sample, Fluence ~ 1.22 x10^{20}

Sample	Low End Loss (µm)	Nominal Loss (µm)	High End Loss (µm)
4	3.00	3.01	3.02
5	3.21	3.35	3.50
6	3.44	3.48	3.52

Unfortunately, due to the large errors in the measured fluence, it is difficult to say at what exact fluence the Mylar was completely eroded. Test 1 offers an upper bound, because it represents the quickest time in the test chamber in which the Mylar fully deteriorated. Therefore, if 1.41 ± .04 x10^{20} atoms/cm^2 represents the theoretical survival limit of the uncoated Mylar, 2.27 ± .24 x10^{20} atoms/cm^2 represents the experimental survival limit of the uncoated Mylar.

The next objective will be to relate these fluence values to an approximate time on orbit. This is difficult because many factors, such as orbital inclination, solar activity, and longitude, affect the amount of atomic oxygen in the atmosphere [9]. However, using the orbit of the International Space Station (400 km altitude, 52 deg inclination), the amount of time in which the Mylar would survive on station can be estimated. The results were found using Spenvis [33], and are shown in Table 7.

Table 7. Survival Time of Uncoated Side of Solar Sail at Station Orbit

	Low Solar Activity	Medium Solar Activity	High Solar Activity
Theoretical, 1.41 $x10^{20}$ atoms/cm^2	59 days	23 days	13 days
Experimental, 2.27 $x10^{20}$ atoms/cm^2	95 days	37 days	20 days

If the solar sail was in a non-optimal orientation where the uncoated side of the sail was exposed to atomic oxygen, it is expected that the sail material would last between a couple weeks to a couple months at station altitude before disintegrating into aluminum dust. Additionally, this estimates the time that any solar sail Mylar that becomes orbital debris will stay in orbit as a threat to other objects.

7.2 Survivability- Coated Side

If the sailcraft ensures that only the protected side of the sail is pointed in the velocity vector direction, and therefore exposed to atomic oxygen, it should be able to survive longer. To determine the survivability of the coated side, samples were exposed in the atomic oxygen chamber for 8 hours, 12 hours, 16 hours, and 24 hours. This ensured a wider variety of fluences to determine how the material degradation changes with different exposure times. During every test the samples' mass was measured before and after to determine if the atomic oxygen was eroding any Mylar. Figure 24 below shows the mass loss for the different fluence values, with error bars representing the standard deviation of the measurements.

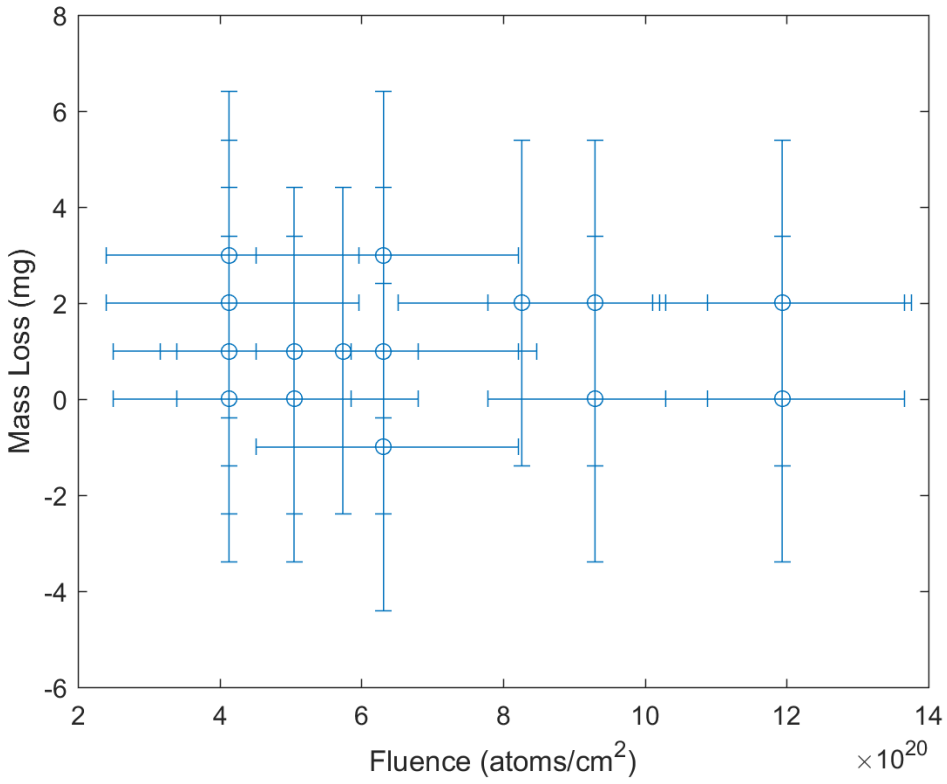

Figure 24. Mass Loss from Sample Coated Side

No value for mass loss has a lower error bar higher than 0, so no sample experienced any definitive mass loss. This agrees with what is known about atomic oxygen resistant coatings. The aluminum coating reacts with the oxygen and creates aluminum oxide, which prevents any atomic oxygen from reaching the Mylar beneath the coating. The only way Mylar can be eroded is through defects in the coating. However, this undercutting is not expected to produce a mass loss measurable by the scale being used, because undercutting happens around pinhole defects.

Instead, an Ambios XP-1 profilometer was used to analyze the amount of undercutting experienced by the material. A sample from a 24-hour test and a sample from a 12-hour test were analyzed with the profilometer. First, Figure 25 shows a 24-hour

sample that was exposed to a fluence of 1.19 x10^{21} atoms/cm^2, in which the profilometer moved from an unexposed region to an exposed region.

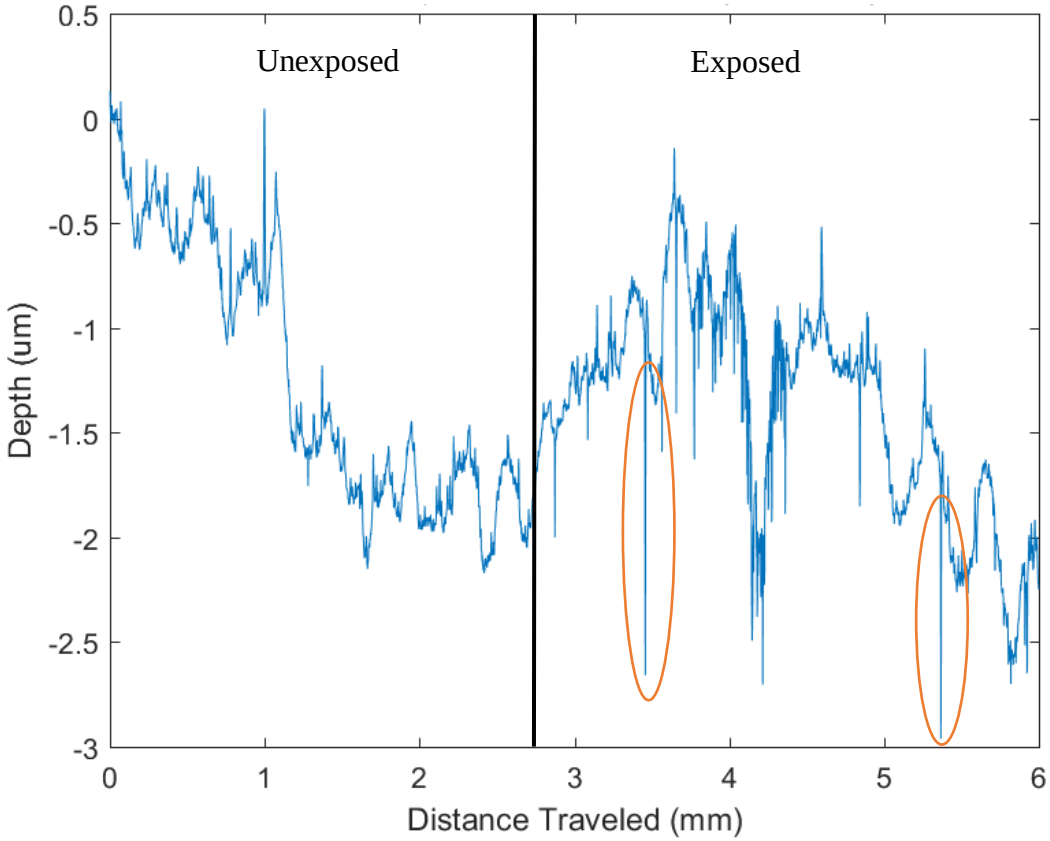

Figure 25. 24-Hour Test Sample, Unexposed Region to Exposed Region, Undercutting Regions Highlighted. Fluence ~ 1.19 x10^{21}

The profilometer scan shows a lot of noise in the unexposed region, likely due to the test stand itself. This noise still exists in the exposed region, however, now a new feature appears: sharp downward lines. Examples of these lines can be seen at ~3.5 and ~5.3 mm along the x-axis. Because these sharp lines don't exist in the unexposed region, they are most likely signs of undercutting. The pictures taken from the profilometer confirm this. Figure 26 shows images of where the profilometer was measuring.

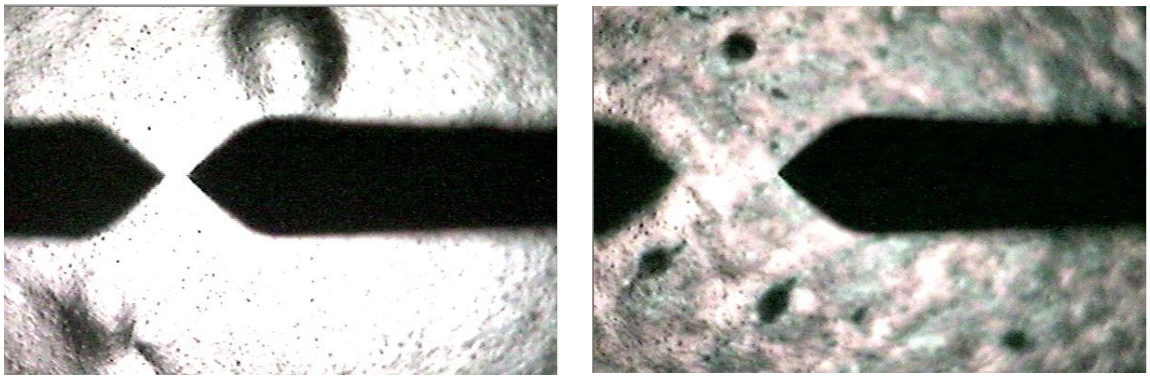

Figure 26. Profilometer Pictures. Left-Unexposed Region. Right-Exposed Region

The clearest difference between the unexposed image and exposed image is the change in reflection, a topic which is covered in Section 7.3. The undercutting is also visible in these pictures. The pinhole defects in the coating can be seen in the unexposed region pictures, they are extremely small, but scattered about the material. In the exposed region picture, some of the defects have grown into larger craters in the material. It is these craters that are being detected in the sharp downward lines in Figure 25. These craters match the theoretical result discussed in Figure 4, where it was shown that atomic oxygen erodes the material directly underneath the defect and ends up widening the defect. Interestingly, some of the defects appear to be affected more than others, as Figure 26 shows only a few of the defects ended up being widened enough to be measurable by the profilometer. Another scan with the profilometer is done with only the exposed region. Figure 27, below, shows the results.

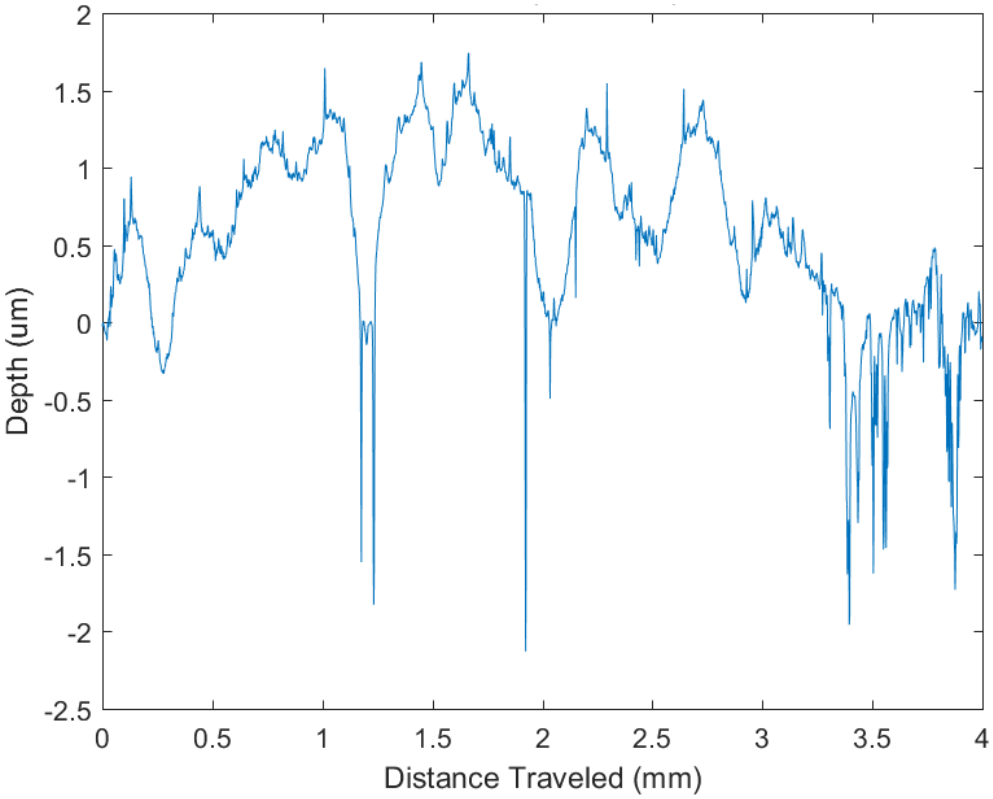

Figure 27. 24-Hour Test Sample, All Exposed Region. Fluence ~ 1.19 x10^{21}

This scan shows more sharp downward lines that are caused by undercutting. From this figure, the number of total defects that turned into undercut craters can be estimated for the entire material. Over the 4 mm of the scan region, approximately 10 craters are detected by the profilometer. This makes 2.5 craters/mm, or 6.25 craters/mm^2. Over an exposure area of 5.06 cm^2, there should be approximately 3000 craters measurable by the profilometer. While these craters are detectable, they are not large. Based on Figure 27, they are approximately 19-35 µm wide and 0.5-3 µm deep. Using a Mylar density of 1.39 g/cm^3, this indicates that 3000 craters would account for approximately 1-10 µg of mass loss. So, the undercutting craters' small size explains why no evidence of them was seen in the mass measurements.

Another important aspect of the craters is that at even at 1.19 x10^{21} atoms/cm^2 of fluence, they are not deep enough to cut through the entire sample. This is crucial for the

analysis, because if the craters did cut through the entire sample, atomic oxygen molecules would be able to hit the bottom aluminum plate of the test stand. Any molecules that struck the bottom plate would bounce off and react with more exposed Mylar. But, in orbit, any atomic oxygen entering a crater that cut through the entire sample would pass through without reacting. So, the fact that the craters don't penetrate the entire sample means that the test results should line up well with orbital results, except for the studied differences due to atomic oxygen energy described in Section 3.2.

To determine when the undercutting starts to be measurable, a sample exposed to atomic oxygen for only 12 hours was scanned as well. The fluence in this test reached 5.05 ±1.76 x10^{20} atoms/cm^2. The results are shown in Figure 28.

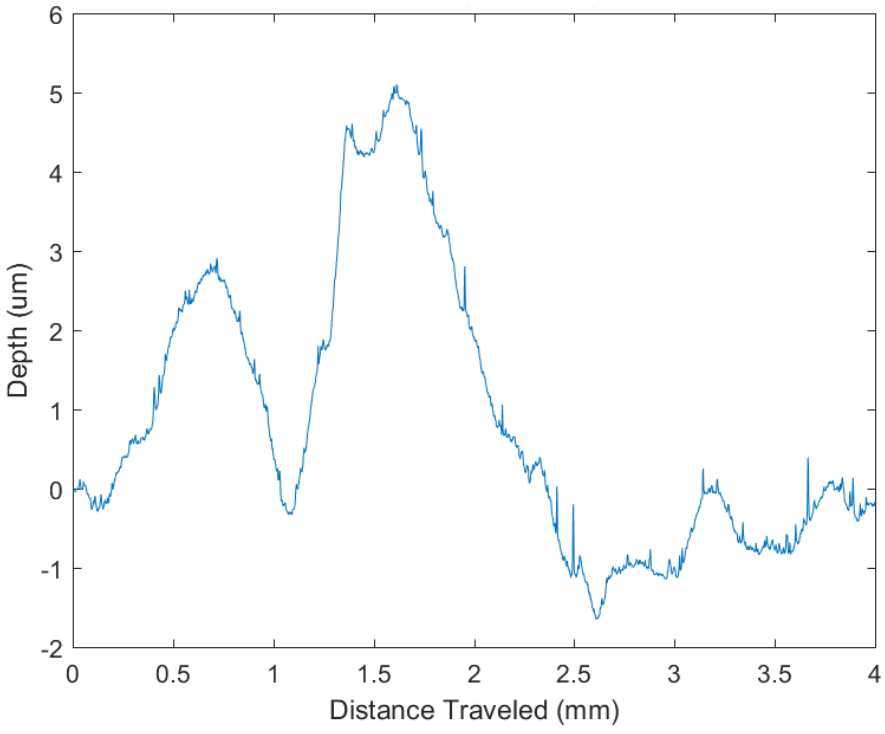

Figure 28. 12-Hour Test Sample, All Exposed Region. Fluence ~5.05 x10^{20}

Interestingly, no sharp downward lines appear in the scan. Multiple scans were taken of different areas of the sample, but no scan showed any evidence of the undercutting as seen before.

For the crater to be measured by the profilometer, it must be at least 2.5 µm wide. Therefore, the fluence of 5.05 ±1.76 $x10^{20}$ atoms/cm^2 was not large enough for any craters to grow to be 2.5 µm wide. If the craters are around 10 µm wide with a fluence of 1.19 $x10^{21}$ atoms/cm^2, and less than 2.5 µm wide with about half of the fluence, the rate of crater growth must be exponential. This is expected, because as the atomic oxygen erodes the Mylar underneath a defect, it widens the defect and thus exposes more Mylar to atomic oxygen. Thus, while no samples in this thesis experienced an atomic oxygen fluence higher than 1.19 $x10^{21}$ atoms/cm^2, it is expected that the undercutting will continue to experience exponential growth, until it eventually erodes all the Mylar.

To determine what effect this undercutting will have on the sail material, the sail as a whole needs to be considered. The sail material used in this thesis will be flown as part of the Planetary Society's Lightsail-2 mission. Figure 29 shows an image of Lightsail-2's sail while it is deployed on the ground. It is known that the sail is pulled with about 3 N of tension [34].

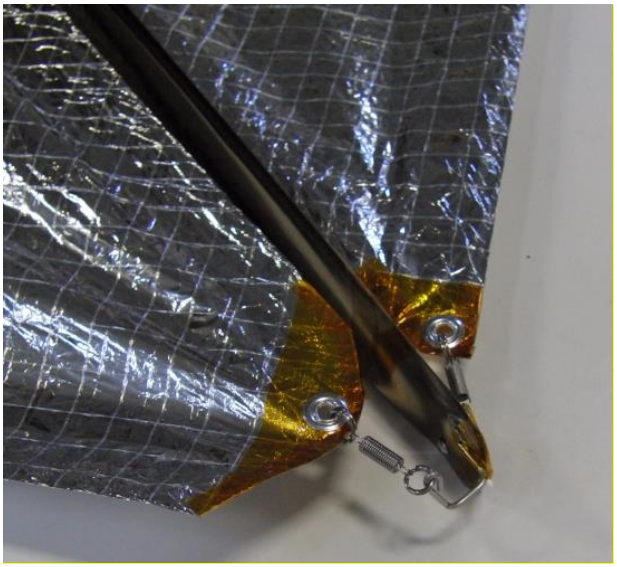

Figure 29. Lightsail-2 Deployed on Ground [34]

The shape of the sail will differ on orbit, because the sail will not be held against gravity. However, the presence of gravity in the image reveals that some areas of the sail, those that are not sagging, experience higher tension than the rest of the sail. Therefore, the distribution of stress along the sail is not uniform. If many erosion craters appear in an area of higher stress, material failure is more likely. Figure 30 demonstrates how this occurs. It shows an example cross-section of the sail material, in which the length is assumed to be 1 mm long and the thickness is 5.3 µm. Present in the cross-section are two straight erosion craters, each 35 µm wide and 3 µm deep. This example represents the results of Figure 27.

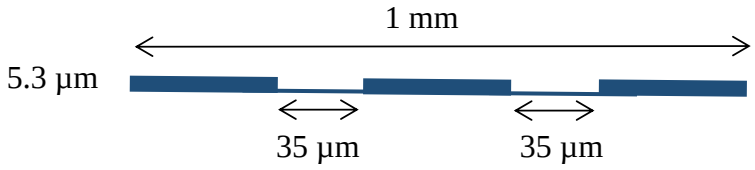

Figure 30. Cross Sectional Area of Sail (not to scale)

The effective cross-sectional area is decreased by the presence of the erosion craters. The cross-sectional area without the craters is 5300 μm^2. With the craters, the cross-sectional area decreases to 5090 μm^2. This represents a 4% decrease in area. Assuming a uniform loading through the cross-section, this would cause at least a 4% increase in the stress experienced. However, the actual increase in stress experienced would likely be far higher due to stress concentrations around the craters. Thus, if this cross-section represented an area of higher tension, this area becomes more likely to fail because of atomic oxygen exposure. And undercutting grows exponentially with increasing fluence, so any fluence higher than the 1.19×10^{21} atoms/cm^2 experienced by Figure 27 will likely produce larger erosion craters, creating greater stress concentrations and leading to a higher chance of structural failure.

The polyester stitches on the coated side of the sail prevent a rip in the sail from propagating. To examine how well they held up to atomic oxygen, the stitches were examined before and after each test. Figure 31 shows a close-up of the stitches on an unexposed sample, as well as on a sample that was exposed for only 7.25 hours, the shortest exposure time for the coated side of the material. It was discovered that the stitches do not survive even after a fluence of 4.13×10^{20} atoms/cm^2.

Figure 31. Stitch Survival. Left- Before Exposure, Right- After Exposure. Fluence ~ 4.13 x 10^{20}

Figure 31 shows that the polyester yarn itself has completely disappeared after atomic oxygen exposure. However, the glue that was holding the polyester stitches in place is still present. This isn't ideal for sail survivability, as with the stitches gone, a small rip in the material is much more likely to develop into a larger one. The exact fluence at which the stitches are eroded away is unknown. However, it is known that the stitches do not survive past 4.13 x10^{20} atoms/cm^2, so that value will be used as the maximum stich survival fluence.

One last observation is that the test samples were more prone to tearing after exposure. Oftentimes, small tears formed while carefully removing the samples from the test chamber. This is likely due to the atomic oxygen undercutting as discussed before, because the undercutting is compromising the structural integrity of the sail material. Thus, for the coated side of the material, atomic oxygen has two main effects for survivability. It makes the sail susceptible to small tears due to the atomic oxygen undercutting of the Mylar. Additionally, any small tears that form have a greater chance of propagating into larger rips because the stitches have been eroded away.

It is difficult to predict at what fluence the entire sail would fail, as that depends on the environment of the mission. However, these observations do give an estimation for two important survivability thresholds: time until the stitches are destroyed and time until significant undercutting is experienced. After either of these occurrences, it becomes more likely that the sail material will fail. For time until stitches are destroyed, the value of 4.13 x10^{20} atoms/cm^2 is used, as previously discussed. For the undercutting threshold, the fluence value of 1.19 x 10^{21} atoms/cm^2 from the 24-hour test is used, in which

significant undercutting was observed by the profilometer. This is likely an over-conservative fluence estimate, because as discussed in Section 3.2, the thermal energy atomic oxygen system produces greater undercutting than orbital atomic oxygen. Table 8 shows the amount of time it would take to reach those fluence thresholds at the International Space Station's orbit. These results were also found using Spenvis [33].

Table 8. Survival Time of Coated Side of Solar Sail at Station Orbit

	Low Solar Activity	Medium Solar Activity	High Solar Activity
Stitches Destroyed, 4.13 x10^{20} atoms/cm^2	155 days	65 days	35 days
Undercutting, 1.19 x10^{21} atoms/cm^2	446 days	188 days	102 days

Even if the coated side of the sail is the only side exposed to atomic oxygen, there will still be survivability concerns. At high solar activity, a solar sail at station orbit would last a maximum of a month before the stitches were eroded by atomic oxygen. This means that after only a month of orbit, a solar sail's risk of failure starts to increase from atomic oxygen exposure. However, a solar sail is more likely to be at a higher orbit, and therefore experience less atomic oxygen. More realistic time frames for a de-orbit sail are discussed in Section 7.4.

7.3 Performance – Optical Parameters

The performance of the solar sail is directly related to the total reflection coefficient, defined as the amount of light neither absorbed nor transmitted after hitting a surface. Performance is also a function of the specular reflection coefficient, defined as the amount of reflected light that is reflected specularly instead of diffusely. These values are used in the solar sail thrust equations (7) and (8).

After being exposed to atomic oxygen, the aluminum coating on the material starts to turn into aluminum oxide. This evolution causes a clear degradation in the optical properties of the aluminum. Figure 32 shows how the surface changed after different levels of atomic oxygen exposure.

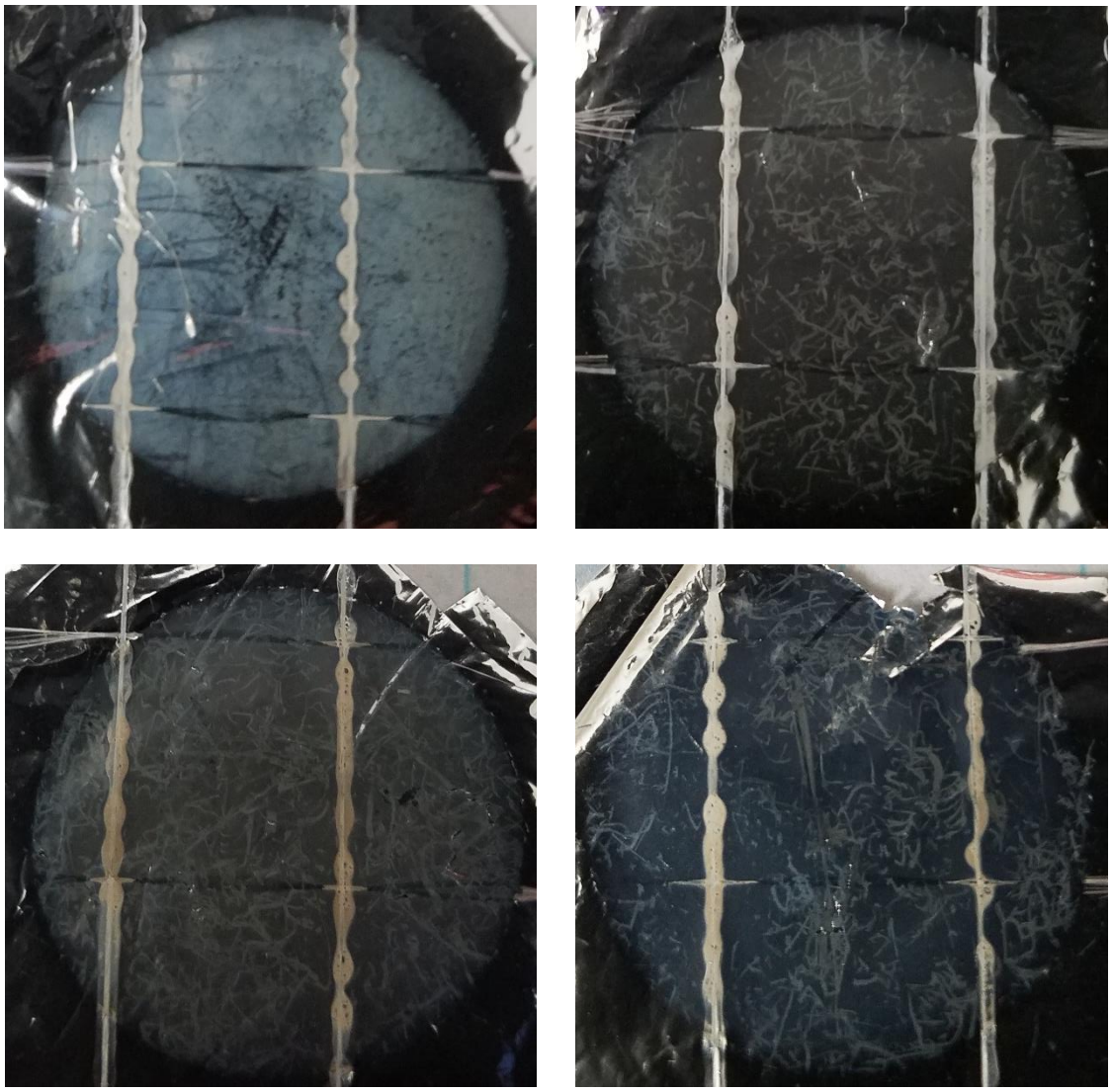

Figure 32. Visual Inspection of Aluminumized Side After Exposure. Top Left- 7 hours. Top Right- 12 hours. Bottom Left- 16 hours. Bottom Right- 22 hours

In all four images, the exposed area is distinct from the unexposed area. The exposed area looks whiter, and contains many small lines that almost resemble scratches.

These lines likely indicate areas of more concentrated aluminum oxide deposits. The whitening effect appears to worsen between the 7 hour and 12 hour exposures. After 12 hours, the size of the aluminum oxide deposits increases for each additional exposure time. Since these effects take away from the mirror-like qualities of the material, it is expected that a clear decrease in total reflection and specular reflection will be measured from the exposed samples.

To measure this expected decrease in total and specular reflection, the reflectometer was used on all exposed samples. Because access to the reflectometer was limited, it was impossible to measure the optical properties of one sample both before and after atomic oxygen exposure. Thus, the exposed samples were compared to two control samples, which were not exposed to atomic oxygen at all.

If a stitch was inside the measurement area of the reflectometer, it would lower the specular reflection value. So, to prevent a stitch from being measured, a guide was used with the reflectometer to ensure that the measurements were being taken from an area between the stiches. The first measurements taken were from the two control samples. On these surfaces, 5-10 measurements were taken without moving the reflectometer at all. Then, the reflectometer was picked up and placed in the same spot again to take another 5-10 measurements. This was done to determine how consistent the reflectometer measurements were on an unexposed surface. Figure 33 shows the results of these measurements on the control samples. The nominal value represents the average of the measurements per one holding of the reflectometer on a sample. The error bar represents one standard deviation of the measurements.

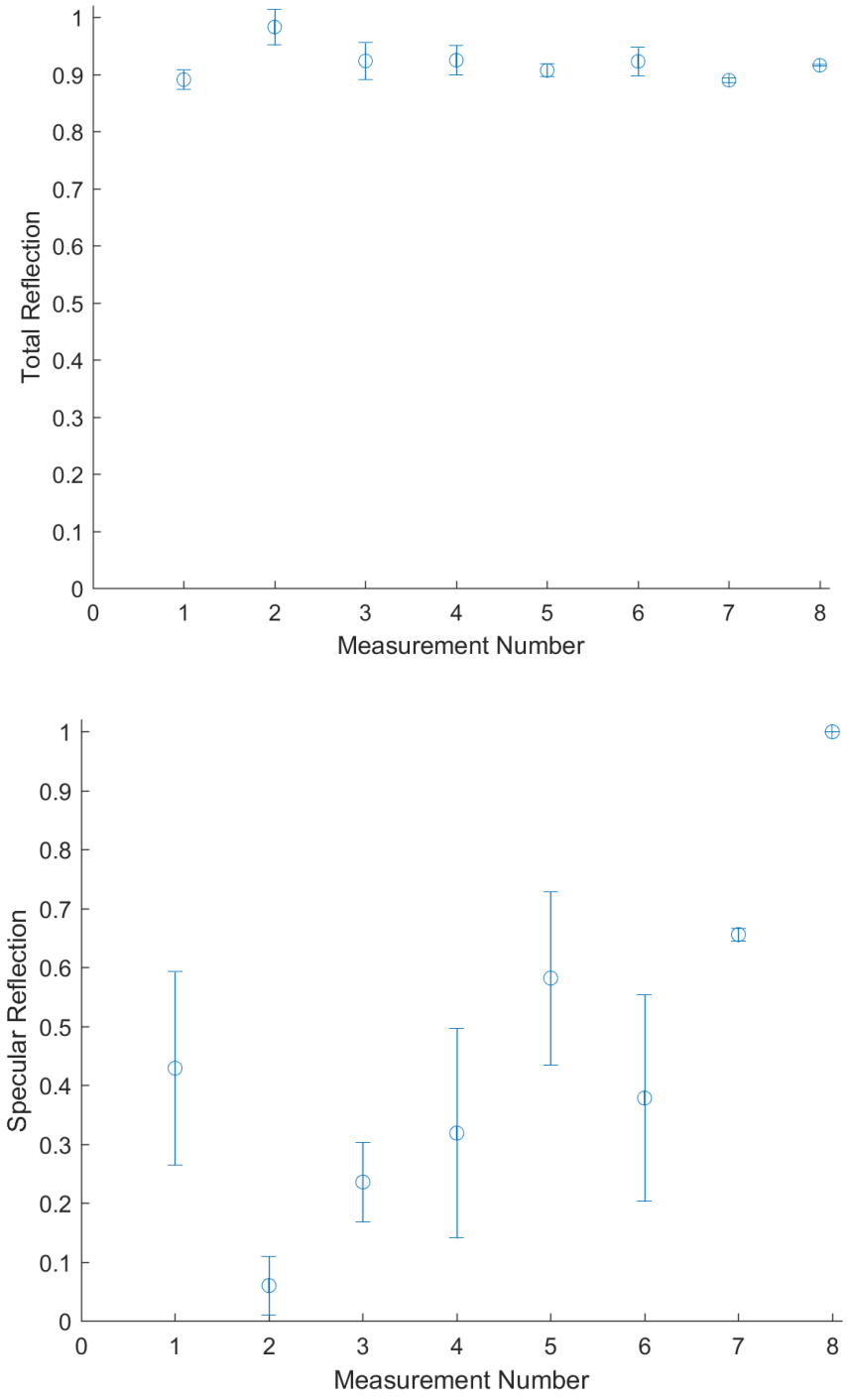

Figure 33. Average Control Surfaces Optical Properties. 1-3 Same Control Sample, 4-7 Different Control Sample, 8 Calibration Mirror

In the total reflection values, every control sample measurement is within 10% of each other. Additionally, the error bar appears to be relatively small. Thus, for total reflection, the values are consistent. The same cannot be said for specular reflection. Both

the individual control samples vary between rounds of measurements, and the error bars are extremely large. This is perplexing, because despite the efforts to keep the reflectometer as steady as possible on the surface of the material, the results still produced a large standard deviation. Also, the material is very mirror-like when observed, so it should have a relatively large specular reflection, which few of the measurements are showing.

The variation in specular reflection results cannot be due to the stiches, because the guide prevented any stitches from being included in the measured area. The variation is also not due to any inherent instrument error. Measurement 8 in Figure 33 shows the results of measuring the calibration mirror. The specular reflection is 1, as expected, and the error bar on both total and specular reflection values is small. Therefore, the variation must be due to wrinkles on the surface of the material. Even though an attempt was made in Section 4.4 to mitigate the effect of wrinkles on a sample, it was not enough.

The wrinkles are a problem due to the way the reflectometer takes reflectance measurements. Test samples must be held solidly against the reflectometer while it is recording the data. However, because the material is extremely thin and flexible, any amount of weight placed on the material causes small wrinkles to appear on the surface. So even on a sample that does not contain any wrinkles normally, the act of measuring the sample causes wrinkles to appear. Additionally, the wrinkles move as the force being applied by the reflectometer shifts. During every sampling round, the device was held as still as possible, but there was likely some small shifting due to human error. This small shifting caused wrinkles to move about on the surface, creating the large variation in specular reflections values.

After this was discovered to be the cause of the large variations, a mitigation strategy was attempted. Taping the backside of the samples to a flat surface seemed to help, but only marginally. In Figure 33, measurements 3 and 7 were taken after the sample was taped to a solid surface. However, any wrinkles that formed during the taping process were made permanent by the tape. So, sometimes the method hindered accurate measurements even further, as shown in measurement 3. However, measurement 7 had a small error bar, and its specular reflection value is relatively high, as expected from this material. Therefore, measurement 7 is the control value used in the rest of the analysis.

After the control samples were measured, every exposed sample was measured 4-8 times. The goal was to be able to see a downward trend in the optical properties that correlated to the amount of fluence the samples received. This trend is expected due to the results from Figure 32. However, the error bars on specular reflection are expected to be large, because of wrinkling on the surface. Figure 34 shows the total reflectivity and specular reflectivity of the exposed samples compared to the experienced atomic oxygen fluence. In total reflection, it is difficult to determine if the value definitively changed, because most of the data points' error bars intersect with the control value. In the specular reflection graph, most of the data points fall below the control value for specular reflection. However, this trend is likely due to wrinkles, as it was seen in Figure 33 that wrinkles both increased the standard deviation of measurements in the specular reflection and dropped the specular reflection down to near zero. Thus, no conclusion can be drawn about specular reflection after exposure to atomic oxygen either. To successfully use the reflectometer, a different measurement strategy needs to be found.

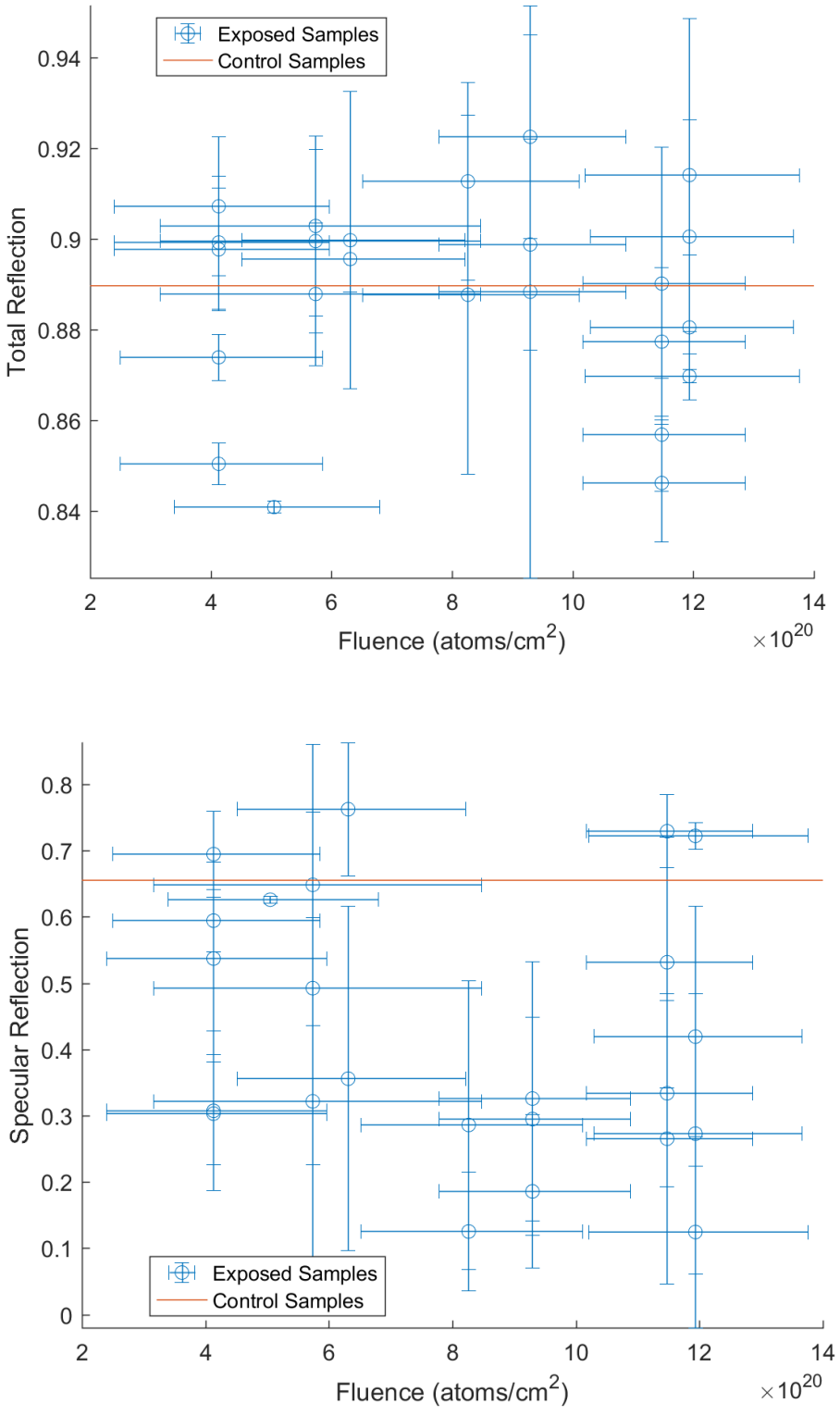

Figure 34. Average Optical Properties of All Exposed Samples

With the remaining amount of reflectometer time, a few choice samples were picked for one last set of measurements. In this set, the reflectometer was continuously adjusted on the surface of the sample until the reflectometer read a relatively high value for specular reflection. It was assumed that a high value for specular reflection meant that no wrinkles were directly inside in the measurement area. One sample chosen for this was a control sample. This is the measurement that led to the small error bar of measurement 7 in Figure 33. Then, three 12-hour exposure samples and two 24-hour exposure samples were chosen due to the samples' large size, which seemed to help make the reflectometer measurements more consistent.

The results of these measurements for total reflectance can be seen in Figure 35 - Figure 38. The results are split up by wavelength to better observe the effect in each wavelength bin. In the figures, there is a clear sign of total reflectance loss from 335 nm to 1100 nm. However, from 1100 nm to 2500 nm, the total reflectance appears to increase or decrease depending on the sample. It appears the aluminum oxide has a similar total reflectance to the aluminum in the infrared wavelengths. However, because total reflectance decreases in the visible wavelengths, and the visible spectrum wavelength bins are weighted higher, the average total reflectance values should drop. This is what is seen in the bottom plot of Figure 38. The average total reflectance drops by a maximum of 5% after exposure to atomic oxygen. However, it is important to note that in the visible wavelengths the total reflectance dropped by about 8%. This drop is likely what it is causing the surface to look whiter after atomic oxygen exposure.

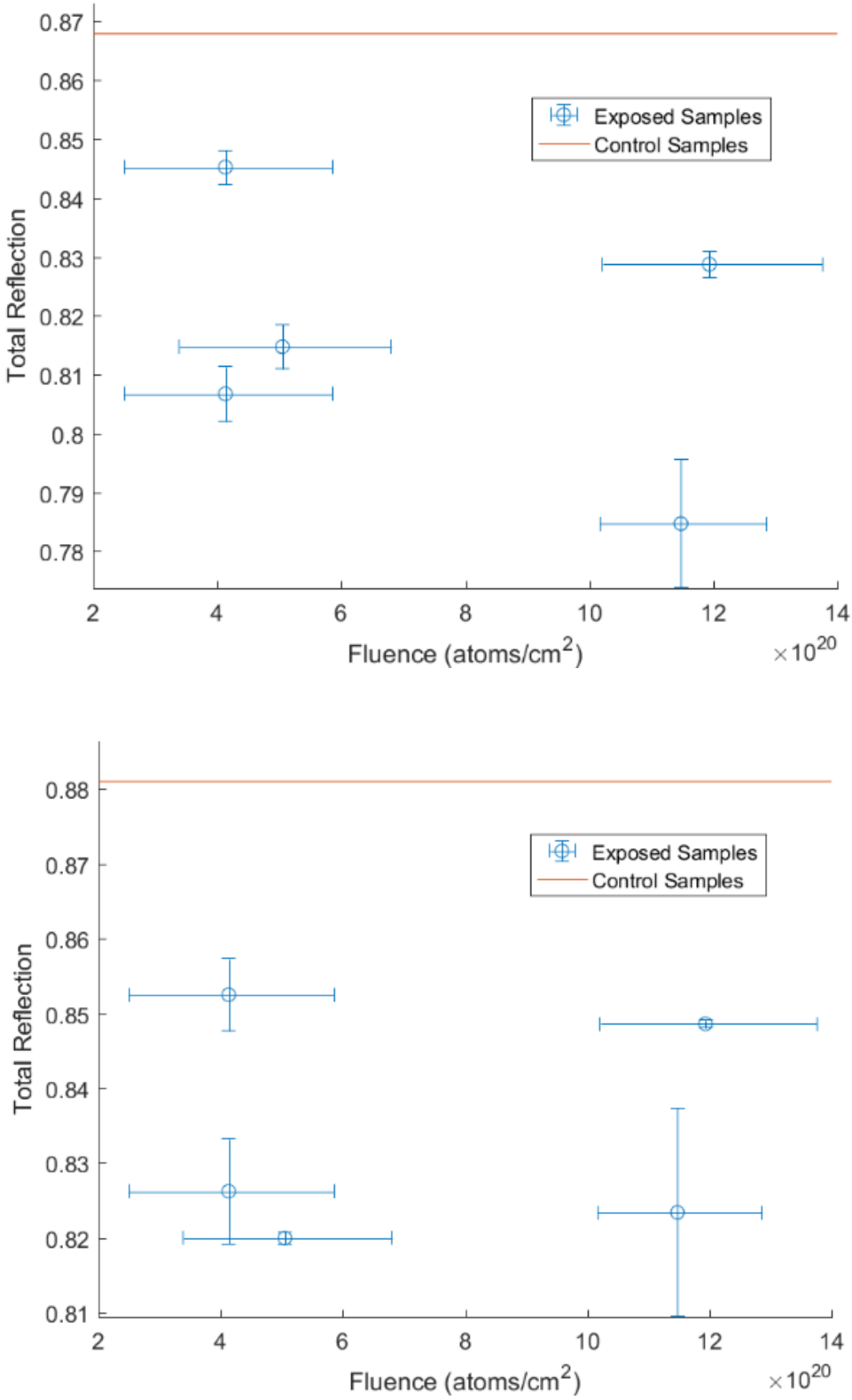

Figure 35. Total Reflection Without Wrinkle Interference. Top: 335-380 nm (UV). Bottom: 400-540 nm (Vis)

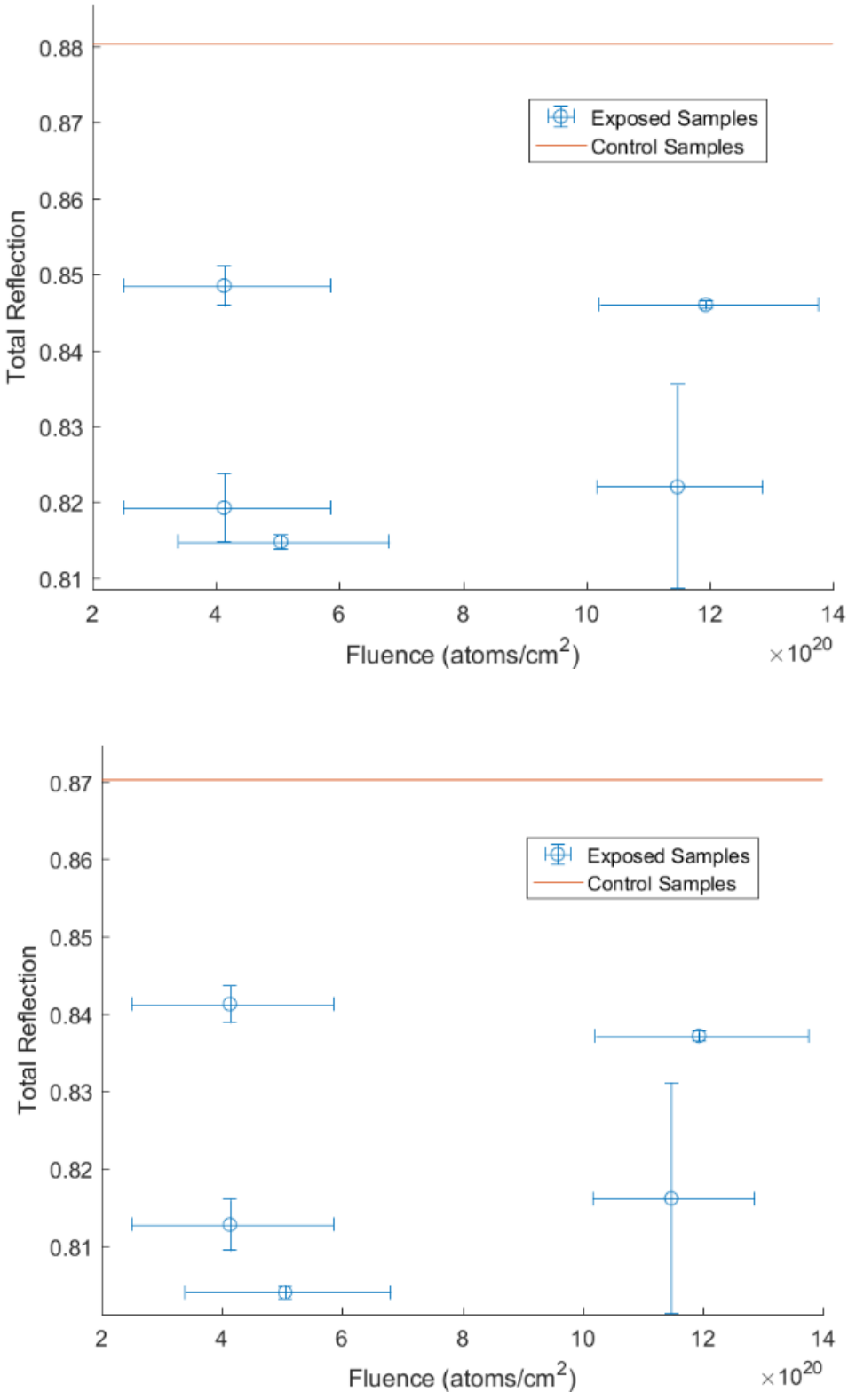

Figure 36. Total Reflection Without Wrinkle Interference. Top: 480-600 nm (Vis). Bottom: 590-720 nm (Vis)

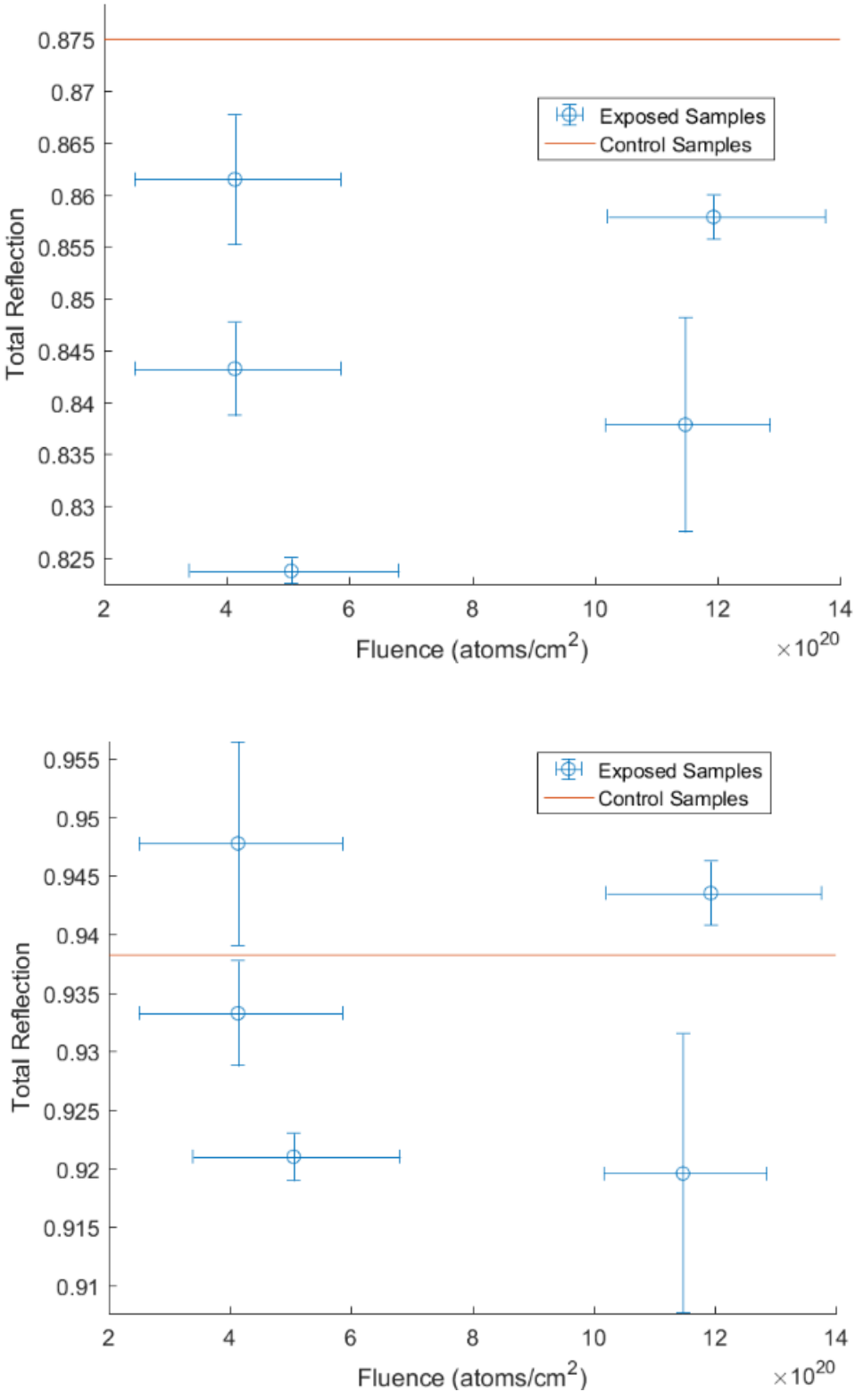

Figure 37. Total Reflection Without Wrinkle Interference. Top: 700-1100 nm (IR). Bottom: 1000-1700 nm (IR)

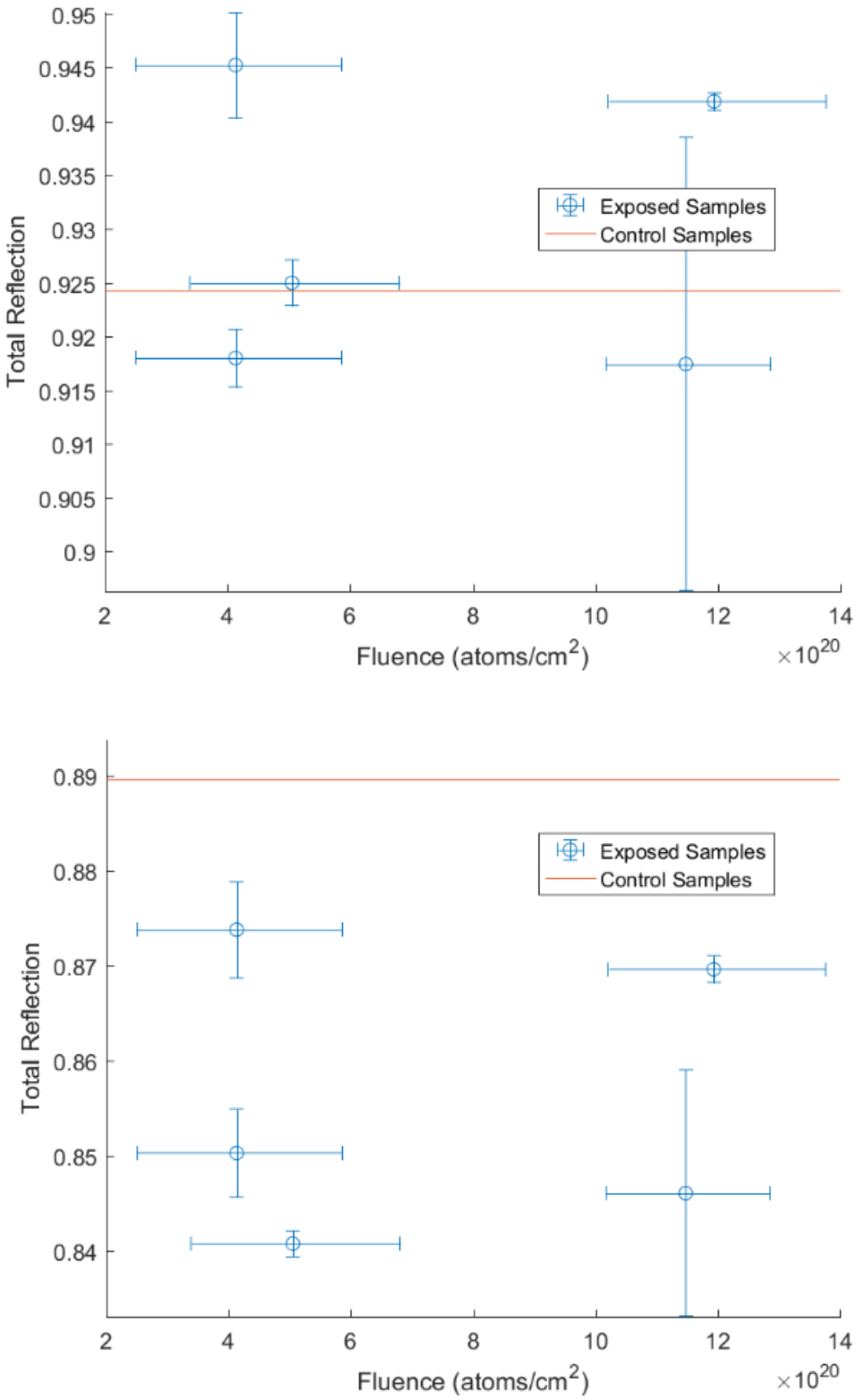

Figure 38. Total Reflection Without Wrinkle Interference. Top: 1700-2500 nm (IR). Bottom: Weighted Average Value

These results also agree with previous experiments done with aluminized films. The degradation of aluminized Kapton has been measured after multiple space-based tests, and often experienced around a 7-9% decrease in total reflectivity after similar atomic oxygen exposure [13]. While the underlying film for this thesis is Mylar instead of Kapton, the oxidation of the aluminum layer is what is being measured, so the different underlying film shouldn't have any effect.

Interestingly, the total reflectance does not appear to have a significant correlation to the amount of atomic oxygen the material was exposed to. This could be because the atomic oxygen fully oxidized the top surface of the aluminum before 12 hours in the chamber had passed. In that case, the reflectance has already reached its worst-case value before approximately 5 $x10^{20}$ atoms/cm^2 of fluence is reached. But, from Figure 32, the samples appear to visually degrade with more exposure time, so that is probably not the case. More likely, the correlation with atomic oxygen fluence is hidden inside the error bars of the measurements. While these error bars are smaller than those in Figure 34, they are still relatively large compared to the average distance from the control line. The size of the error bars is likely due to different levels of wrinkling on the surface that can be experienced while the reflectometer is held against the material. If measurements were made with more assurance that wrinkles were not interfering, a correlation between degradation and atomic oxygen fluence would be expected.

Figure 39 - Figure 42, below, show the specular reflectivity results from the last round of measurements. The results appear to be more consistent than those found in Figure 34.

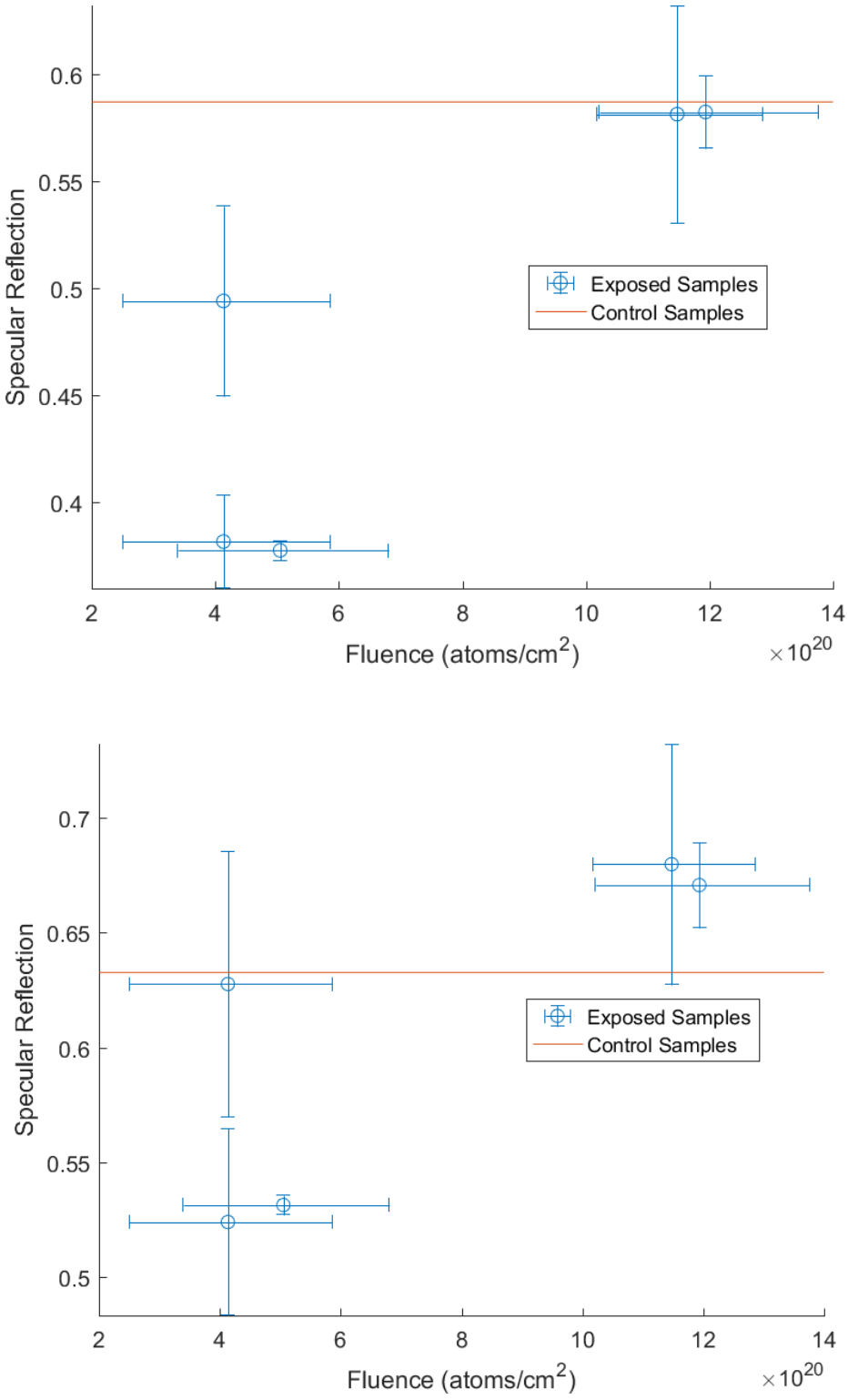

Figure 39. Specular Reflection Without Wrinkle Interference. Top: 335-380 nm (UV). Bottom: 400-540 nm (Vis)

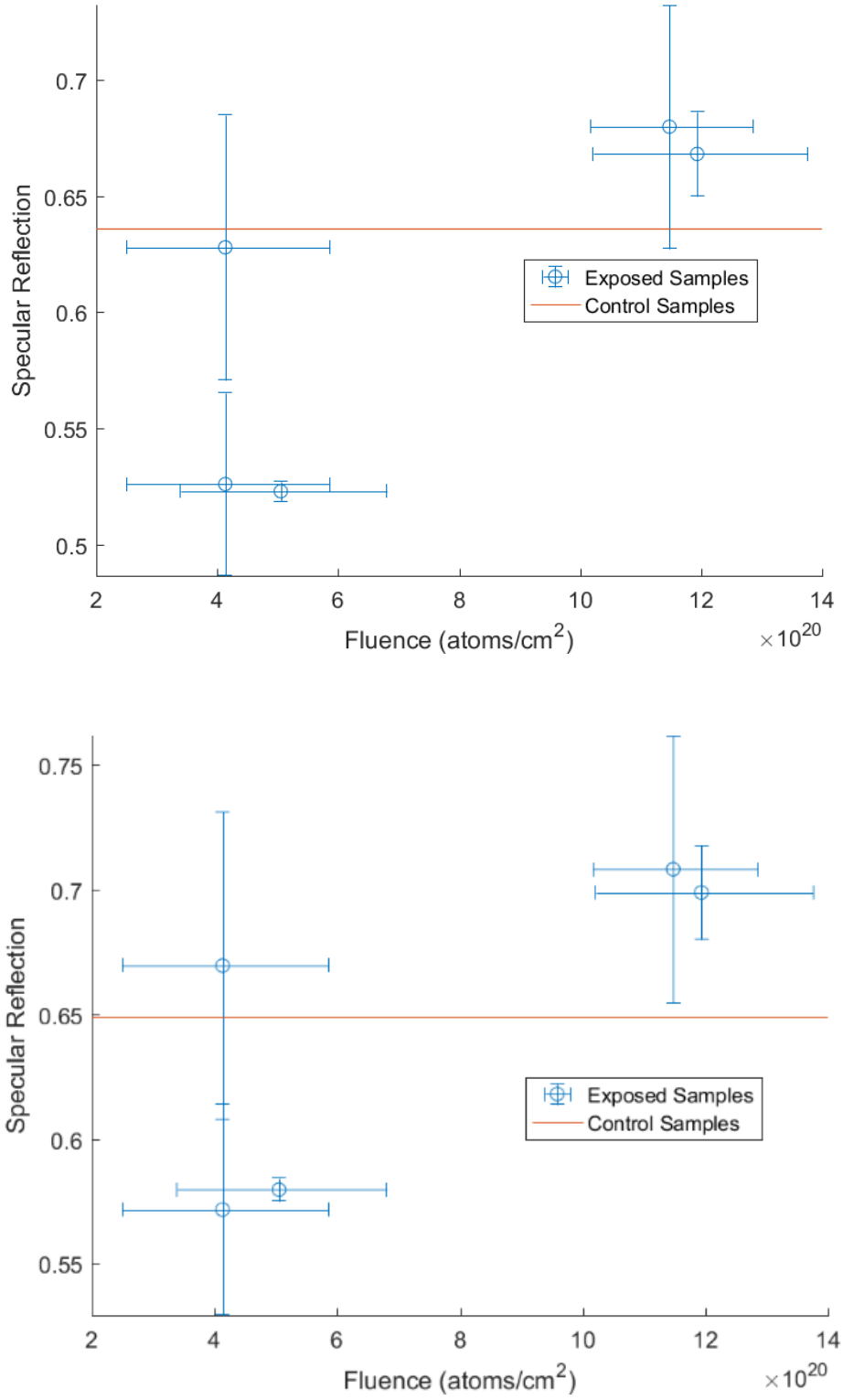

Figure 40. Specular Reflection Without Wrinkle Interference. Top: 480-600 nm (Vis). Bottom: 590-720 nm (Vis)

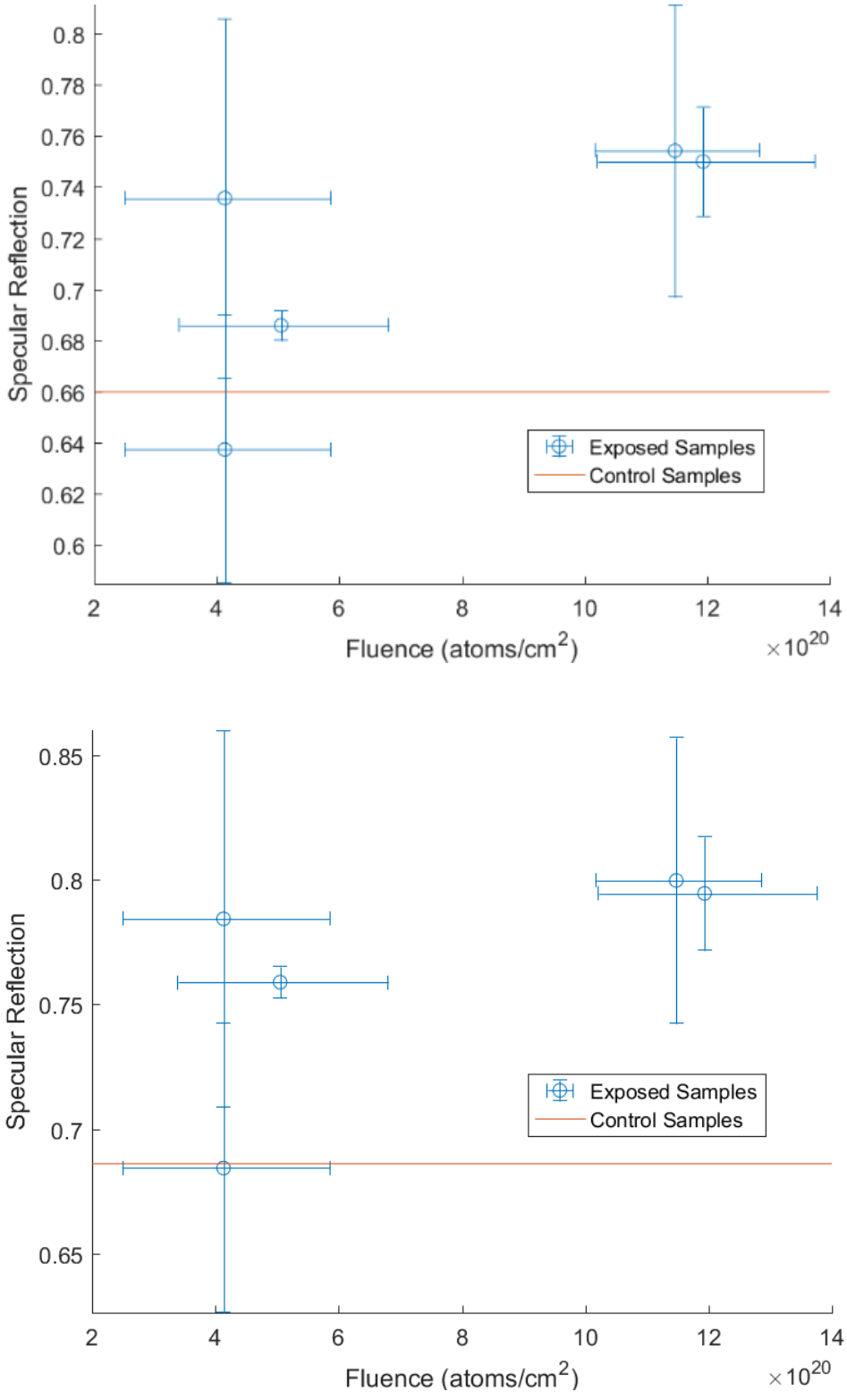

Figure 41. Specular Reflection Without Wrinkle Interference. Top: 700-1100 nm (IR). Bottom: 1000-1700 nm (IR)

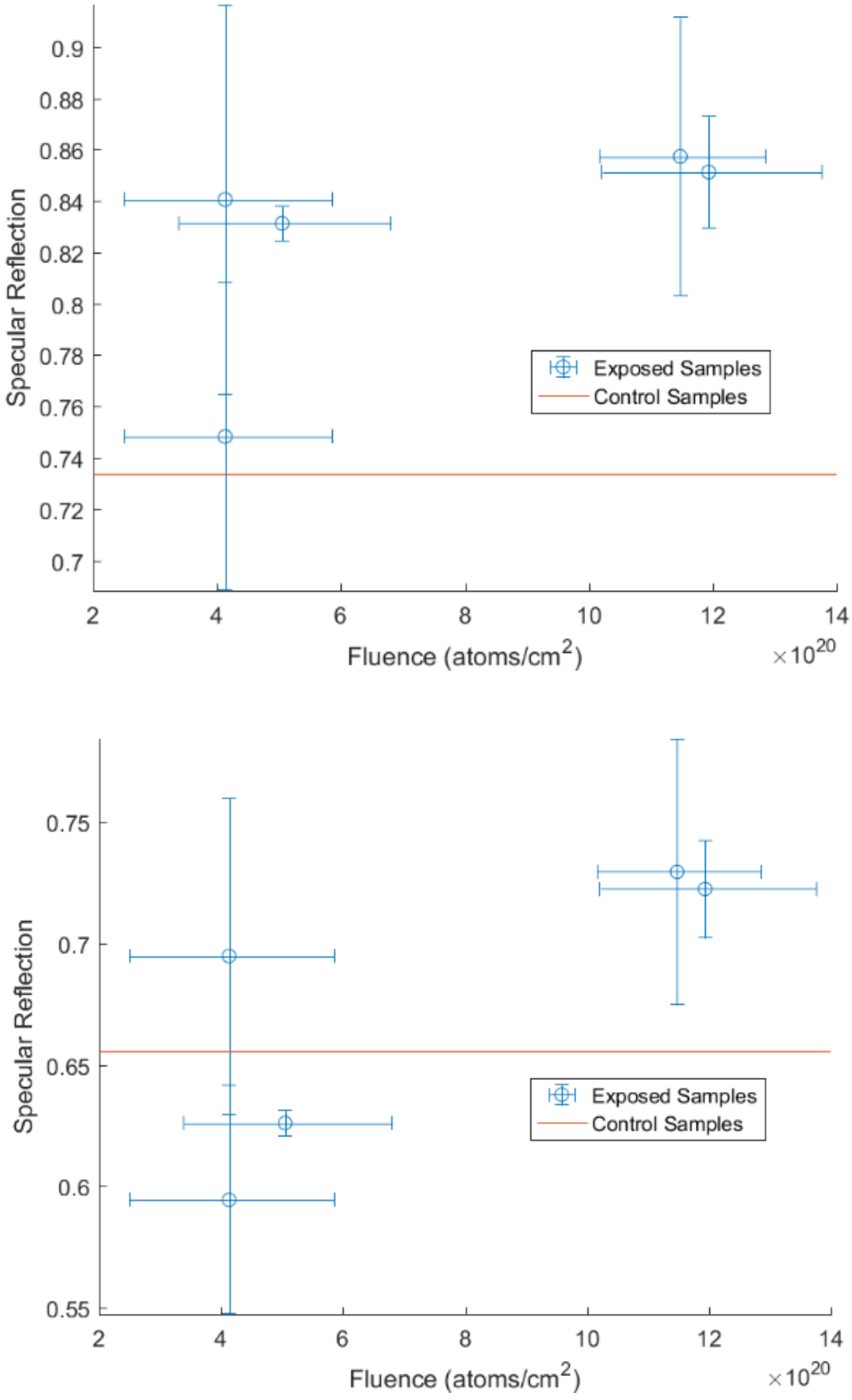

Figure 42. Total Reflection Without Wrinkle Interference. Top: 1700-2500 nm (IR). Bottom: Weighted Average Value

There is agreement among the measurements that specular reflection degraded in the ultraviolet wavelengths, shown in the top plot of Figure 39. In the visible spectrum, the results are split between whether the specular reflection increased or decreased. However, the whitening of the material from Figure 32 suggests that the specular reflection in the visible wavelengths should have seen a definitive decrease in value. Wrinkles are still the most likely reason for why this decrease isn't seen in the visible wavelengths. Because it is impossible to determine the wrinkle level of the samples while being measured, it is probable that different wrinkle levels between the control and the exposed samples caused some of the exposed samples to have a larger visible wavelength specular reflectivity than the control.

Interestingly, in the infrared wavelengths, the results are more conclusive. Four out of five of the measurements suggest that specular reflectivity increased after atomic oxygen exposure. Therefore, it seems likely that the specular reflection for aluminum oxide is lower than aluminum in the visible and ultraviolet wavelengths, but higher than aluminum in the infrared wavelengths. This increase in reflectivity in the infrared wavelengths will bring up the average specular reflectance, while the decrease in the ultraviolet wavelengths will bring it down. The overall result should be that the average specular reflection value in this solar sail material doesn't change significantly after atomic oxygen exposure. The bottom plot of Figure 42 demonstrates that a few samples experienced an increase in average specular reflection, and a few experienced a decrease. But in all cases, the error bar is close to the control value.

There are no published papers regarding the specular reflection change in aluminized polymer films. This is likely because the bulk of atomic oxygen research on

thin film polymer materials has been done in the context of using the material for thermal control. In thermal control applications, only the total reflectance matters, not the specular reflectance. This means no comparison to outside work is possible for these specular reflectance measurements.

Overall, for specular reflection, the effect of any wrinkles in the material far exceeds the effect of any atomic oxygen exposure. In fact, the control samples might not represent the actual optical properties of Lightsail-2. The best way to measure the optical parameters experienced by Lightsail-2 would be to use the reflectometer on the sail material while it is deployed on the flight deployment mechanism. Then, any wrinkles that appear will also be present while the spacecraft is in orbit. Naturally, this is not an option for the purposes of this thesis. What can be seen in this thesis is around a 5% decrease in average total reflection values after exposure to atomic oxygen. Average specular reflection appears to experience no definitive significant change. In both cases, a correlation with fluence wasn't found, likely because wrinkles have an outsized effect on the measurement results.

7.4 Performance – Orbit Trajectories

To better contextualize what effect the optical parameter change will have on the de-orbiting ability of a solar sail, an example sailcraft will be used along with the sail angle determination algorithm defined earlier. For this sailcraft, the ballistic coefficient will be assumed to equal 0.1. This simulates the idea that the 32 m^2 Lightsail-2 is being used to de-orbit a satellite weighing 320 kg. The orbit will start circular at 800 km in altitude and zero degrees inclination. Ideally, the total and specular reflectivity values

would be modeled to degrade over time as the satellite experiences more atomic oxygen exposure. However, because a correlation between optical degradation and fluence was never found, the full trajectory will be made assuming that the reflectivity values never change over time. But, multiple cases will be run with different levels of degradation to provide an upper bound for how heavily the degradation influences the de-orbit time of the sailcraft.

To shorten the code run time, a couple of changes were made to the initial optimization code discussed in Section 5.3. First, rather than directly integrating the equation of motion defined in equation (12), the modified equinoctial set of orbital parameters was integrated instead. This is commonly done during low-thrust optimization codes to save integration time [35].

Additionally, to prevent the code from running an fminsearch function at every time step of the Matlab's ode45 solver, the trajectory is split into two regions: the drag-dominated and the SRP-dominated. In the SRP-dominated region, the full optimization code was run for only one period of the initial orbit. For the duration of this orbit, the optimal sail angle was paired with the eccentric anomaly of the orbit and stored. Then, in all future calculations, the sail angle was found by matching the current eccentric anomaly to the stored eccentric anomaly. This assumes that the best sail angle at a given point on an SRP-dominated orbit will be the same for all future orbits. The inaccuracies caused by this approximation will predominantly be at the perigee of the orbit, where the drag force will increase as the perigee decreases. The changing drag force means a different sail angle would have been found by the optimization. However, during the

SRP-dominant region of the trajectory, the maximum de-orbit inducing acceleration occurs during apogee, so the errors caused by the simplification should be minimal.

Whenever the sail is below 500 km in altitude in medium solar activity, it is in the drag-dominated region. In this region, the sail angle is set to zero to maximize the effect the drag force has on the vehicle. This is in line with the results of Figure 14, where it was found that below ~500 km, the drag force magnitude becomes dominant. Thus, when perigee drops to below 500 km, drag will begin to create a large acceleration that will bring down the apogee of the orbit. In the high solar activity case, all trajectories below 550 km are considered drag-dominant, while in the low solar activity case the boundary is set to 450 km. These values are also in line with the results from Figure 14. The overall result should be similar to that seen in Figure 20.

The first case studied will be with the values measured from the control sample in the previous section: r = 0.89 and s = 0.65. Figure 43 shows the sail angle over time, for both the entire trajectory and for a short time period during the SRP dominant region.

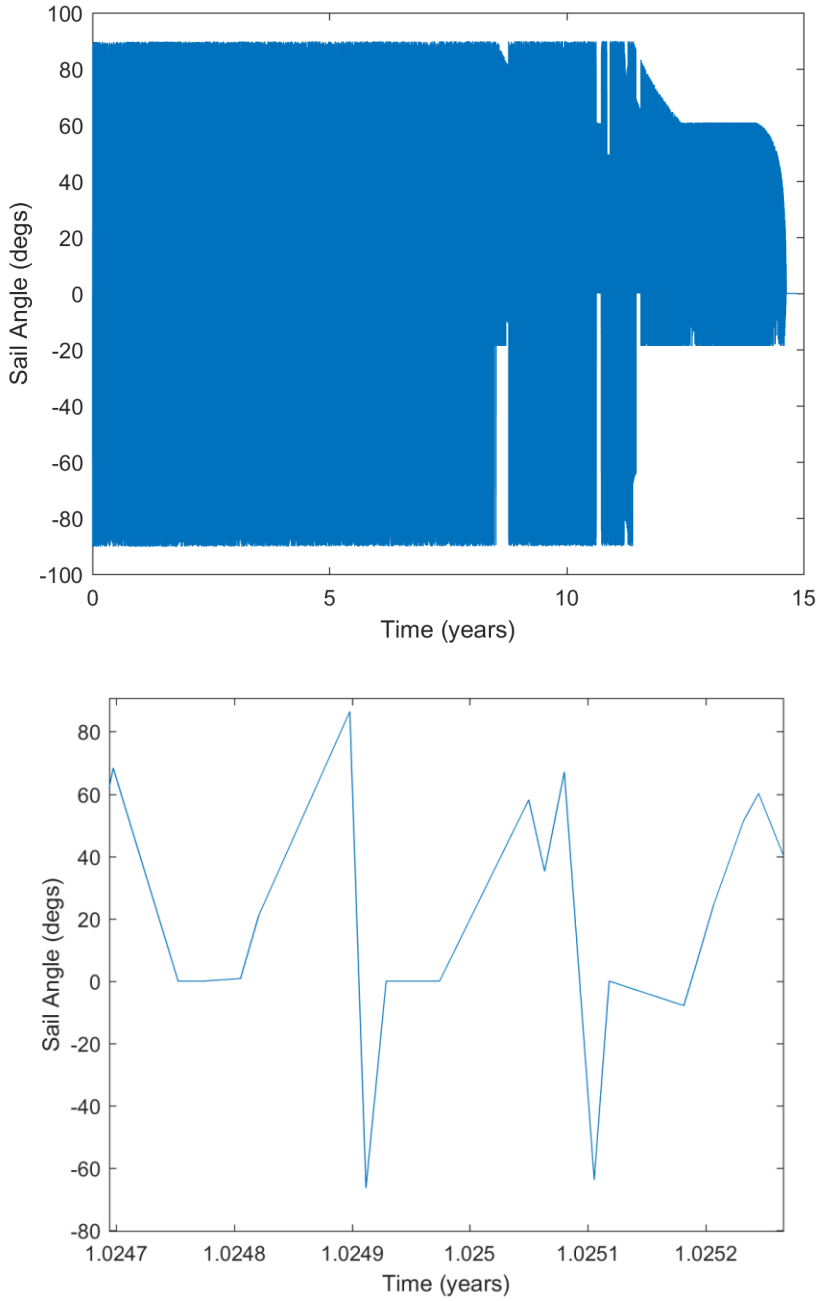

Figure 43. Sail Angle For BC=.1, Non-Degraded Reflectance, Medium Solar Activity Top- Entire Trajectory, Bottom- Oscillations within SRP Dominant Region

The bottom plot in Figure 43 shows that, similar to Figure 19, the sail angle oscillates greatly while the satellite is in the SRP-dominant region of the orbit. However, it does not appear to oscillate between 90 and -90 degrees as expected. This is due to the large time steps taken by the ode-solver, which limit the resolution of the plot. However,

the top plot confirms that this oscillation does indeed occur between 90 and -90 degrees during the SRP-dominant region. The top plot also shows that once perigee is low enough for drag to become more dominant, the sail angle remains closer to zero. This agrees with the previous results, shown in Figure 19. Lastly, Figure 43 shows that the total time until sail de-orbit was around 15 years. Thus, this satellite would pass the NASA and ESA requirement of de-orbiting within 25 years upon mission termination. Whereas without the solar sail, a different means of propulsion would have been needed. Figure 44 below shows the altitude of the spacecraft over time as well as the total accumulated fluence.

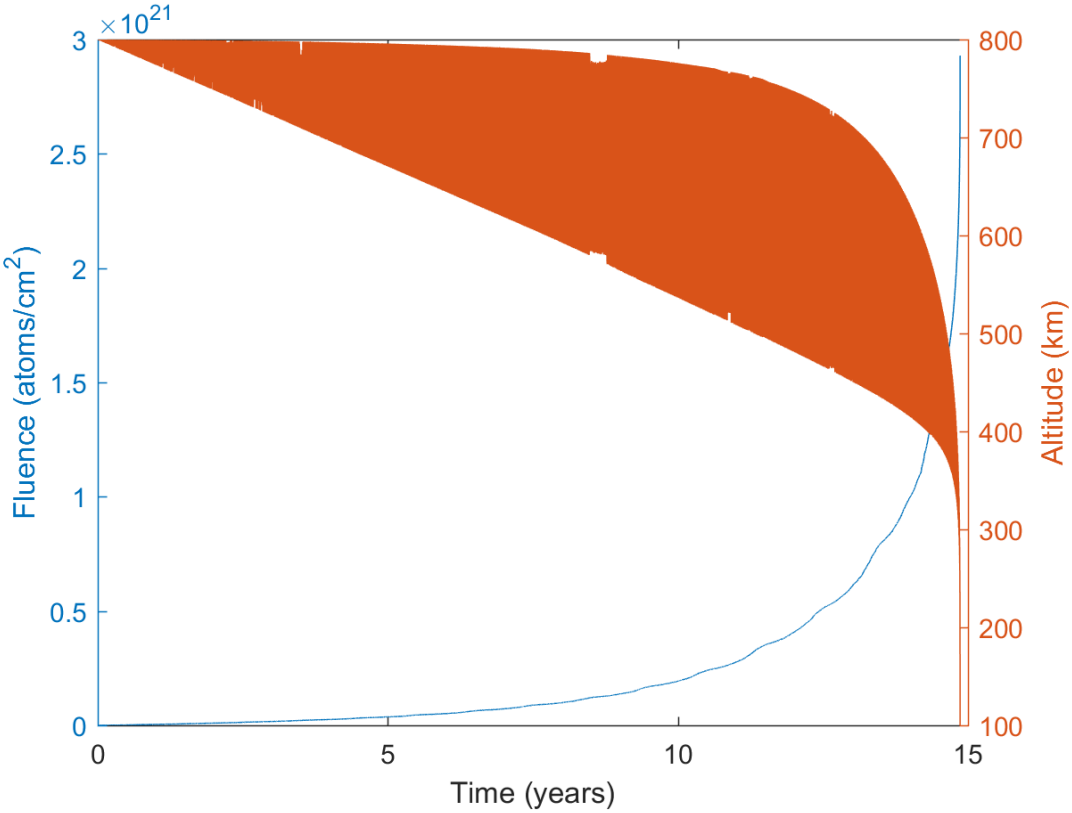

Figure 44. Altitude and Fluence for BC=.1, Non-Degraded Reflectance, Medium Solar Activity

The altitude graph looks very similar to Figure 20 in that the perigee of the orbit decreases first, while apogee remains constant before dropping later. The fluence graph also looks similar to Figure 20, with a slow increase while the sail is at a higher altitude

and a sharp increase as apogee begins to fall. These similarities to the previous results mean that the inaccuracies caused by the simplifications related to finding the sail pointing angle are minimal.

It is interesting to compare the fluence gained in this simulation to the fluence of atomic oxygen from the lab tests. At 2.27 $x10^{20}$ atoms/cm^2 the uncoated side of the Mylar was destroyed. This fluence would have been reached at around 10 years into this mission. Meanwhile, the longest test with a fluence of 1.19 $x10^{21}$ atoms/cm^2 showed significant undercutting of the Mylar material. This fluence would have been reached a couple hundred days before the object is considered re-entered. At this point, even if the solar sail was lost due to undercutting, the satellite would re-enter due to drag relatively quickly, as the orbital altitude was already below 400 km.

The next test case is run with the same satellite characteristics, but with high solar activity as defined in Table 3. This means the atmosphere will expand outwards, which has two effects: increasing drag due to a rise in atmospheric density, and increasing atomic oxygen flux. The altitude and fluence plot for this satellite is shown in Figure 45.

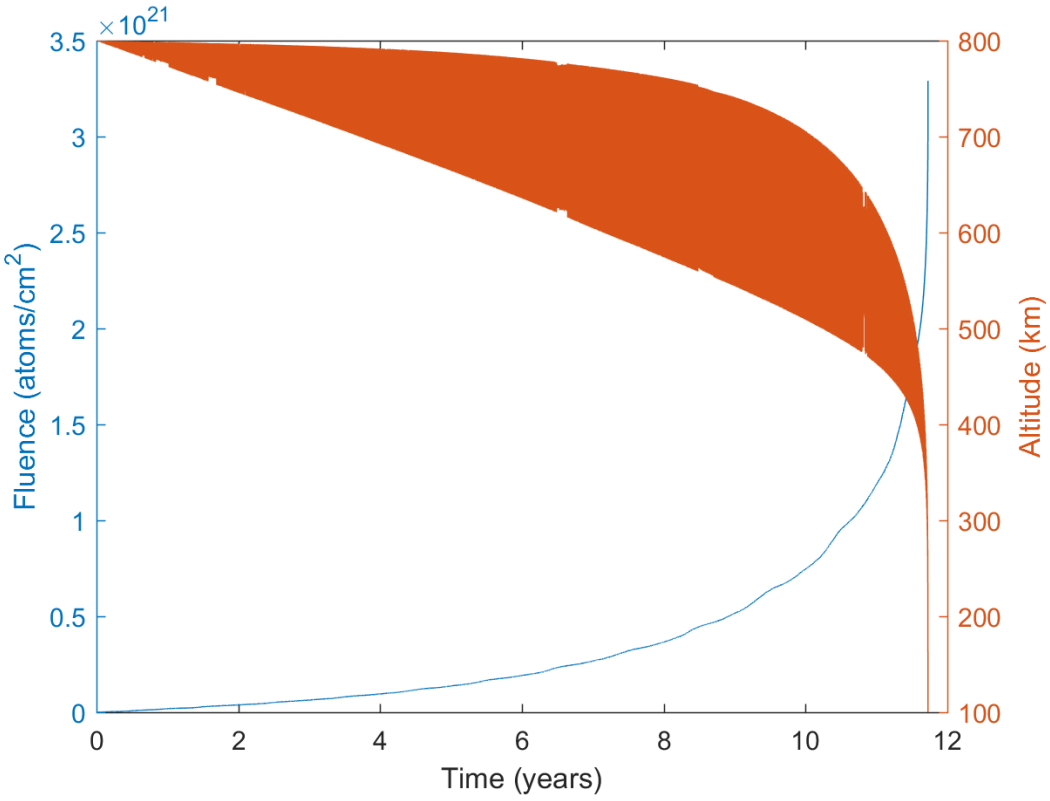

Figure 45. Altitude and Fluence for BC=.1, Non-Degraded Reflectance, High Solar Activity

In this test case the satellite took around 12 years to de-orbit. This is lower than during medium solar activity, as expected due to the increase in drag force. Additionally, the fluence line indicates that the uncoated Mylar would have been destroyed after approximately 6 years, and the undercutting fluence was reached a couple hundred days before de-orbit, similar to the previous test case. This means that the fluence thresholds were reached quicker with high solar activity than with medium solar activity. This is expected because, as seen previously, the atomic oxygen flux increases with solar activity. The significant undercutting fluence is still only reached once the satellite is in a low enough orbit for the sail to not be necessary to finish the mission.

The next test case is with low solar activity. This case should take the longest, as the drag force will be at its lowest value. Figure 46 below shows the altitude and fluence for this test case.

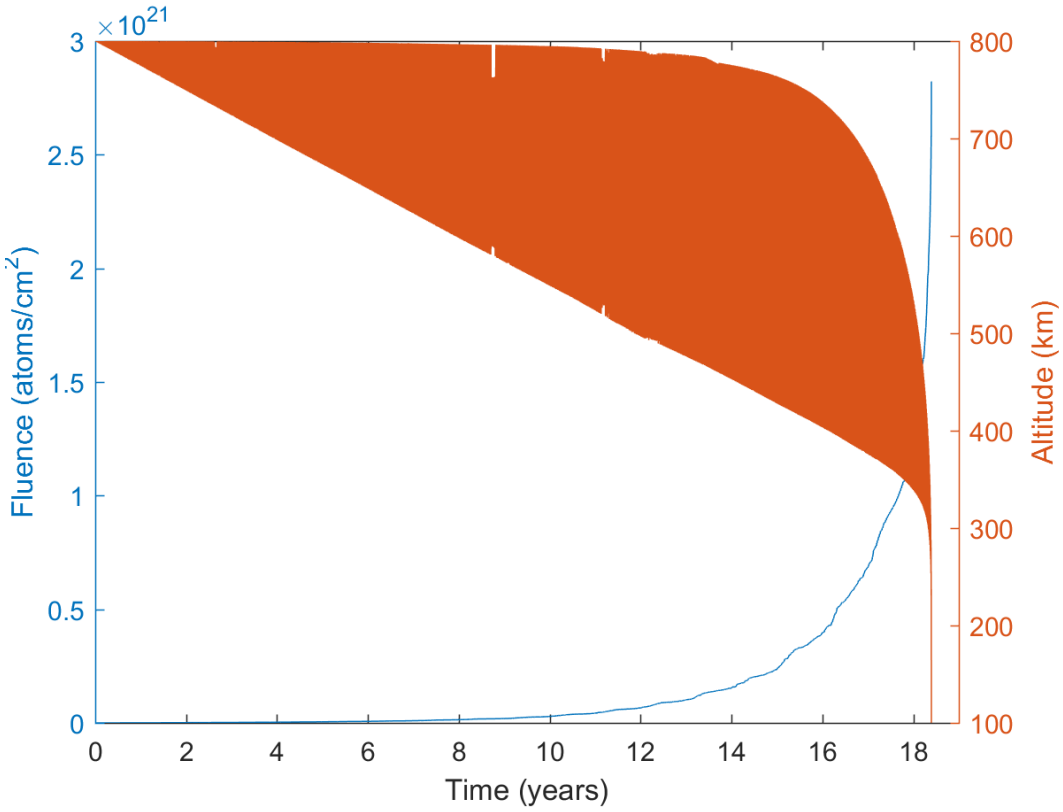

Figure 46. Altitude and Fluence for BC=.1, Non-Degraded Reflectance, Low Activity

The satellite took around 18 years to de-orbit, longer than with medium solar activity, as expected. The atomic oxygen would have destroyed the uncoated Mylar within 15 years, while the coated side would have experienced significant undercutting a few hundred days before de-orbit, similar to the previous two cases.

These test cases all represented a solar sail that never experiences any optical degradation. Another set of tests are run with a 5% drop in total reflectivity. This represents the total reflectivity degradation after atomic oxygen exposure that was seen in Figure 38. Meanwhile, specular reflectivity is kept constant as there was no definitive

degradation in that parameter. The next set of tests was run with a 5% drop in both total and specular reflectivity. This represents the worst-case data point seen in both Figure 38 and Figure 42. One last run shows the de-orbit time assuming a perfectly reflecting solar sail, where r=s=1. The represents the sail performance with the commonly assumed reflectance values for a solar sail [21]. Table 9 shows the de-orbit time for every test case. Also shown is the time taken to reach uncoated side destruction, stitch destruction, and significant undercutting.

Table 9. Sail De-Orbit Times for Different Levels of Solar Activity and Degradation

Solar Activity	r	s	Time to De-Orbit (yrs.)	Uncoated Side Destroyed (yrs.)	Stitches Destroyed (yrs.)	Significant Undercutting (yrs.)
Low	1	1	14.6	12.0	13.0	14.3
Low	.89	.65	18.2	14.6	16.0	17.8
Low	.84	.65	18.5	14.9	16.2	18.1
Low	.84	.60	19.0	15.2	16.7	18.6
Medium	1	1	12.3	8.9	10.2	11.9
Medium	.89	.65	14.9	10.4	12.0	14.3
Medium	.84	.65	15.2	10.6	12.3	14.6
Medium	.84	.60	15.5	10.6	12.3	14.8
High	1	1	9.7	5.7	7.2	9.2
High	.89	.65	11.7	6.4	8.3	11.0
High	.84	.65	11.9	6.6	8.4	11.2
High	.84	.60	12.3	6.8	8.6	11.5

In every case, lowering the values for specular and total reflectivity meant a longer time to de-orbit. However, the change between the measured reflectance values is overall insignificant, less than a year difference between optimal measured reflectivity versus worst-case measured reflectivity. The difference between the perfectly reflecting sail material assumption versus the actual measured reflectance produces a more significant change, decreasing the de-orbit time by 2-4 years. Thus, it is important to have a good approximation for the actual reflectance of the sail material, as the assumption that the sail material is perfectly reflecting can produce misleading results about the sail performance. Similarly, it is important to consider the expected solar activity level, as it can vary the amount of time taken to de-orbit by about ±3 years. In every test case the fluence required to produce significant undercutting of the material was reached around half a year before the satellite re-entered. So, in every test case the fluence was only reached once the solar sail was already low enough in altitude that drag would be able to bring down the spacecraft without the solar sail.

This is good news for the idea of using solar sails as de-orbit devices. The exposure to atomic oxygen will not significantly degrade the performance of the solar sail material. Having a good approximation of the solar activity level and the actual reflectance of the sail material matters more than atomic oxygen exposure when it comes to de-orbiting a LEO satellite. Additionally, during nominal operation the atomic oxygen will not be able to significantly undercut the protective aluminum coating before the solar sail is able to complete the majority of its mission.

There are two main concerns from Table 9. First, the solar sail will not be able to complete its de-orbit mission if the uncoated side spends a long period of time exposed to

the incoming atomic oxygen. The sail will always be destroyed years before the satellite is low enough for drag to bring down the satellite on its own. Second, the stitches are always destroyed by the atomic oxygen before the sail has de-orbited the satellite. This means that the probability of a minor hole evolving into a tear, which can cause total failure, increases in the middle of the mission.

7.5 Solar Sail Design

This study about atomic oxygen degradation of solar sail material reveals a few important design aspects to consider when creating solar sails to be used in LEO. First are the two concerns from Table 9. With proper attention, these concerns are easily mitigated. To protect the uncoated side from the incoming atomic oxygen, a reliable sail deployment method coupled with an adequate sail control law should be able to ensure that the uncoated side is never exposed. The destruction of the stitches is best mitigated by material selection. A stitch material that is more resistant to the effects of atomic oxygen could help ensure that the stiches remain present for the entire mission of a de-orbit sail.

There is also an important trade-off that should be considered. Equation (7) describes how the best performance of a solar sail is achieved when $r = s = 1$. This causes the term in front of the normal SRP thrust to equal 2. However, if specular reflection is zero, the term in front of the SRP pressure force is 1 instead. So, having a sail material with a large specular reflectivity is important, as it can potentially double the amount of thrust a solar sail generates. Section 7.3 revealed that the wrinkle level of a material has a significant impact on the material's specular reflectivity. To ensure that the sail material has a high specular reflectivity, a solar sail should be pulled tightly while deployed to

minimize the number of wrinkles on the surface. But, section 7.2 revealed that the solar sail experienced a loss in structural integrity due to atomic oxygen undercutting. If a sail is under a large amount of tension, this loss of integrity could cause structural failure. Thus, in LEO sail design, it is important to understand the effects of undercutting on the specific sail material being used, and balance the increased performance with the increased risk of structural failure by having a high-tension sail.

8.0 Future Work

To better simulate the LEO environment, there are a few changes that could be made to the test apparatus. First, using an atomic oxygen generator that produced highly directional atomic oxygen with orbital energy would better simulate the atomic oxygen seen in orbit. In this thesis, this change would have significantly affected the results of the undercutting study, since it is known that thermal energy systems typically create a larger amount of undercutting than is seen in orbit [19]. Additionally, in LEO, ultraviolet light from the sun often discolors spacecraft material [36]. If solar sail material is exposed to ultraviolet light, this discoloration would likely produce an additional degradation of total and specular reflectivity. An ultraviolet simulation apparatus already exists for the atomic oxygen chamber used [9]; unfortunately, it was not in service during the time of this thesis.

A better method of measuring the reflectivity of the surface would have generated more accurate results regarding the degradation due to atomic oxygen. The most accurate method to predict on-orbit reflectivity values would be to measure the sail while it is deployed on the flight deployment mechanism. Otherwise, an apparatus that places the sail material under an equivalent amount of tension as the flight deployment mechanism would better simulate the number of wrinkles present on the surface.

A large portion of research could be done on the wrinkles in the solar sail alone and how they impact the reflectivity of the material. Developing a method of predicting the specular reflection of a material that considers the wrinkling of the surface would significantly benefit solar sail mission designers as they calculate how much thrust the solar sail will be able to generate. Also, determining a method of reducing the number of

wrinkles on the sail surface while not increasing the risk of structural failure of the sail material would lead to better performing solar sails.

A similar analysis as this thesis could be used on other types of solar sail material as well. If the type of coating is changed, the oxidation of the coating from atomic oxygen would need to be re-examined to determine how atomic oxygen changes the optical properties of the material. However, using other types of thin film polymer material as the base of the solar sail would impact the erosion mass loss study as well as the undercutting study.

Lastly, the structural degradation of the material due to atomic oxygen exposure would be better measured with a tensile test. The area comparison used does not consider the resultant stress concentrations that would form around the erosion craters. The most accurate estimation of the structural impact of atomic oxygen would be with a directional atomic oxygen system and a tensile test with the sail material.

9.0 Conclusion

Solar sail material equivalent to that used in Lightsail-2 was provided to the Aerospace Department at California Polytechnic State University by Ecliptic Enterprises. An isotropic, thermal energy atomic oxygen system was used to estimate the degradation of this solar sail material from the atomic oxygen environment. The degradation effects were separated into two different categories: survivability and performance.

In survivability, it was found that the uncoated side of the material would only survive on the order of weeks if exposed to atomic oxygen at an orbit similar to the International Space Station. For the coated side of the material, it was found that atomic oxygen eroded the stitches designed to prevent tear propagation. The required fluence on orbit was estimated to occur after 1-5 months at station altitude. Additionally, profilometer measurements showed that the sail material experienced a significant amount of undercutting as a result of the atomic oxygen exposure. This undercutting was estimated to cause significant structural integrity damage to the sail material after approximately 6-15 months at station altitude.

For performance of the sail material, it was discovered that the amount of wrinkling present on the surface of the sail material affected the reflectivity of the material more than atomic oxygen exposure. This created difficulty when measuring the reflectivity of the sail material with a reflectometer. However, when the effect of wrinkling was limited as best as possible, it was found that the average total reflectivity dropped around 5% as a result of atomic oxygen exposure. Specular reflectivity appeared to decrease in the ultraviolet wavelengths, but increased in the infrared wavelengths, so the average value did not change after atomic oxygen exposure. In neither specular nor

total reflection was the reflectivity found to have a correlation with the fluence experienced. This was contrary to expectations, because a longer exposure time led to a clear visual degradation of reflectivity on the material's surface. The lack of a correlation was attributed to the effect of wrinkles on the material that were created by holding the reflectometer to the surface.

Lastly, a trajectory determination algorithm was developed that would find the best pointing angle for a solar sail in a simplified 2D orbit case with drag and SRP. This algorithm was implemented to predict how the atomic oxygen degradation would affect a solar sail designed to de-orbit a LEO satellite. Without any degradation, the satellite took between 12-18 years to deorbit from an initial circular orbit of 800 km, depending on the solar activity. If the total reflectivity was dropped 5%, the satellite took approximately three more months to de-orbit in all solar conditions. With a 5% drop in both total and specular reflectivity, the satellite took approximately six more months to de-orbit. Meanwhile, the difference between the actual measured reflectivity versus an assumed perfect reflectivity caused a 2-4 year de-orbit time difference. The solar activity level changed the de-orbit time by around ±3 years. Thus, knowing the solar activity level and estimating the actual reflectance values of the solar sail is more significant than atomic oxygen degradation with regards to the de-orbit time of a solar sail deployed to bring down a LEO satellite.

In all test cases run, the amount of fluence required to cause significant undercutting of the solar sail material was reached a few hundred days before re-entry. At that altitude, it is probable that even if the solar sail were to fail, the satellite would still re-enter due to drag within the 25 years that is required by NASA and ESA. However, the

structural integrity calculation used does not reflect the effect of stress concentrations around erosion craters, which would decrease the amount of fluence required to cause the sail to fail. Additionally, if any uncoated side of the sail material was exposed to atomic oxygen, it would be destroyed approximately halfway into the mission. Therefore, it is recommended that the deployment mechanism and control law are able to ensure that atomic oxygen never reaches the uncoated side of the solar sail. On the coated side, the stitches, which protect against sail tearing, would be destroyed by atomic oxygen significantly prior to mission completion. Finding a stitch material that is more resistant to the effects of atomic oxygen would mitigate the risk of sail failure caused by the destruction of the stitches. Lastly, for solar sail performance, it is best to subject the solar sail to high tension while deployed to increase the specular reflectivity of the material. However, this could expedite the destruction of the sail because atomic oxygen undercutting compromises the structural integrity of the material. Thus, future LEO solar sail mission designers must balance the increased performance with increased chance of failure when considering the sail's tension.

This research was done to assess the risks associated with using solar sails in LEO with regards to the atomic oxygen environment. If solar sails are used more often, in missions like LEO de-orbiting trajectories, confidence in solar sailing technology will grow. As solar sails build up heritage, they are more likely to be utilized in the inter-planetary missions that would most benefit from solar sailing.

REFERENCES

[1] M. MacDonald, "Solar Sailing: Applications and Technology Advancement," in *Advances in Spacecraft Technologies*, InTech, 2011.

[2] B. Dunbar, "Technology Readiness Level," NASA, October 2012. [Online].

[3] J. L. Anderson, "NASA's Nanosail-D 'Sails' Home -- Mission Complete," 29 November 2011. [Online].

[4] J. Davis, "Lightsail Workshop Recaps Lessons Learned From Test Mission," The Planetary Society, July 2015. [Online].

[5] J. Davis, "Signed, sealed but not delivered: LightSail 2 awaits ship date," 20 March 2017. [Online].

[6] D. S. Romagnoli, "De-Orbiting Satellites in LEO Using Solar Sails," *22nd International Symposium of Space Flight Dynamics*, 2011.

[7] B. F. J. B. R. R. U. Geppert, "The 3-Step DLR-ESA Gossamer Roadmap to Solar Sailing," 2010.

[8] ESA, "Sailing Satellites Into Safe Retirement," 20 December 2013. [Online].

[9] M. J. Glicklin, "Development of a Ground Based Atomic Oxygen and Vacuum Ultraviolet Radiation Simulation Apparatus," California Polytechnic State University, San Luis Obispo, 2012.

[10] D. G. Timothy Minton, "Dynamics of Atomic-Oxygen Induced Polymer Degradation in Low Earth Orbit," in *Chemical Dynamics in Extreme Environments*, Singapore, World Scientific Publishing Co., 2001.

[11] K. d. G. S. M. Bruce Banks, "Low Earth Orbital Atomic Oxygen Interactions with Spacecraft Materials," NASA, Gleen Research Center, 2004.

[12] A. Doan, "Synergistic Effects of Atomic Oxygen and Ultraviolet Radation Exposure on Various Spacecraft Materials," California Polytechnic State University, San Luis Obispo, 2013.

[13] R. Reddy, "Effect of Low Earth Orbit Atomic Oxygen on Spacecraft Materials," *Journal of Materials Science*, 1995.

[14] A. S. S. M. K. d. G. Bruce Banks, "Atomic Oxygen Undercutting of Protected Polymers in Low Earth Orbit," *Journal of Spacecraft and Rockets, Vol 41.*, 2004.

[15] T. Svitek, *Stellar Exploration CDR*, The Planetary Society.

[16] Planetary Society, "FAQs and Stats: All About Lightsail," [Online].

[17] Grafix Plastics, "Mylar Film and Sheet Properties," 2007. [Online]. [Accessed April 2017].

[18] D. W. S. T. K. d. A. S. S. M. Bruce Banks, "Comparison of Atomic Oxygen Erosion Yields of Materials at Various Angles and Impact Energies," NASA, Glenn Research Center, 2006.

[19] K. d. S. R. F. D. Bruce Banks, "Prediction of In-Space Durability of Protected Polymers Based on Ground Laboratory Thermal Energy Atomic Oxygen," NASA, Lewis Research Center, 1996.

[20] A. E. 2089-00, "Ground Laboratory Atomic Oxygen Interaction Evaluation of Materials for Space Applications," ASTM International, West Conshohocken, PA, 2006.

[21] G. Greschik, "Direct Thrust Efficiency for the L'Garde Sail Surface with a Linear Reflectivity Model," in *Advances in Solar Sailing*, Springer Praxis Books, 2014.

[22] D. Rind, "Do Variations in the Solar Cycle Affect Our Climate System?," January 2009. [Online].

[23] B. P. Barbara Ryden, "Blackbody Radiation," in *Foundations of Astrophysics*, San Francisco, Pearson, 2011.

[24] W. N. K. V. M. V. Alejandro Frangi, "Multiscale Vessel Enhancement Filtering," Image Sciences Institute, University Hospital Utrecht, 1998.

[25] D.-J. Kroon, "Hessian Based Frangi Vesselness Filter, v1.11," 2 March 2010. [Online].

[26] H. Curtis, Orbital Mechanics for Engineering Students, Third Edition, Elsevier, 2014.

[27] N. Hall, "Shape Effects on Drag," 5 May 2015. [Online].

[28] H. L. M. C. C. R. A. Seppala, "Geomagnetic Activity Signatures In Wintertime Stratosphere Wind, Temperature, and Wave Response," *Journal of Geophysical Research Atmospheres,* March 2013.

[29] M. W. Michael Souder, "Solar Sail Technology for Nanosatellites," *AIAA,* 2008.

[30] Mathworks, "R2017a Documentation: ode45," 2017. [Online].

[31] MathWorks, "R2017a Documentation: fminsearch," 2017. [Online].

[32] K. d. G. B. B. K. C. Deborah Waters, "Changes in Optical and Thermal Properties of the MISSE 2 Peace Polymers and Spacecraft Silicones".

[33] ESA, "SPENVIS Project: AO," Royal Belgian Institute for Space Aeronomy, Version 4.6.8.3181. [Online].

[34] A. Diaz, Interviewee, *Lightsail-2, Ecliptic Enterprises.* [Interview]. 4 May 2017.

[35] A. V. R. Kathryn F. Schubert, "Minimum-Time Low-Earth Orbit to High-Earth Orbit Low-Thrust Trajectory Optimization," *Advances in Astronautical Sciences,* Vols. 13-926, 2013.

[36] V. L. Pisacane, The Space Environment and Its Effect on Space Systems, American Institute of Aeronautics and Astronautics, 2008.